Convection-Parameterized and Convection-Permitting Modelling of heavy precipitation in decadal simulations of the greater Alpine region with COSMO-CLM

Alberto Caldas-Alvarez[1], Hendrik Feldmann[1], Etor Lucio-Eceiza[2,3], and Joaquim G. Pinto[1]

[1]Institute of Meteorology and Climate Research (IMK-TRO), Karlsruhe Institute of Technology (KIT), Karlsruhe, 76131, Germany.
[2]Institute of Meteorology, Freie Universität Berlin (FUB), Berlin, 14195, Germany.
[3]Deutsches Klimarechenzentrum (DKRZ, German Climate Computing Center), Hamburg, 20146, Germany.

Correspondence to: Alberto Caldas-Alvarez (caldalv.alberto@gmail.com), Hendrik Feldmann (hendrik.feldmann@kit.edu)

Abstract. Heavy precipitation is a challenging phenomenon with high impact on human lives and infrastructures and thus a better modelling of its characteristics can improve its understanding and simulation at climate time scales. The achievement of Convection Permitting Modelling (CPM) resolutions ($\Delta x < 4$ km) has brought relevant advancements in its representation . However, further research is needed on how the very high resolution and switching-off of the convection parametrization affect the representation of processes related to heavy precipitation. In this study, we evaluate reanalysis driven simulations for the greater Alpine area over the period 2000-2015 and assess the differences in representing heavy precipitation and other model variables in a CPM setup with a grid-size of 3 km and a Regional Climate Model (RCM) setup at 25 km resolution using the COSMO-CLM model. We validate our simulations against high-resolution observations (EOBS, HYRAS, MSWEP, and UWYO). The study presents a revisited version of the Precipitation Severity Index (PSI) for severe event detection, which is a useful method to detect severe events and is flexible to prioritize long lasting events and episodes affecting typically drier areas. Furthermore, we use Principal Component Analysis (PCA) to obtain the main modes of heavy precipitation variance and the associated synoptic Weather Types (WTs). The PCA showed that four WTs suffice to explain the synoptic situations associated with heavy precipitation in winter, due to stationary fronts and zonal flow regimes. Whereas in summer, 5 WTs are needed to classify the majority of heavy precipitation events. They are associated with upper-level elongated troughs over western Europe, sometimes evolving into cut-off lows, or by winter-like situations of strong zonal circulation. The results indicate that CPM represents higher precipitation intensities, better rank correlation, better hit rates for extremes detection, and an improved representation of heavy precipitation amount and structure for selected events compared to RCM. However, CPM overestimates grid point precipitation rates, which agrees with findings in past literature. CPM systematically represents more precipitation at the mountain tops. However, the RCMs may show large intensities in other regions. Integrated Water Vapour and Equivalent Potential Temperature at 850 hPa are systematically larger in RCM compared to CPM in heavy precipitation situations (up to 2 mm and 3 K respectively), due to wetter mid-level conditions and an intensified latent heat flux over the Sea. At the ground level, CPM emits more latent heat than RCM over land (15 W m^{-2}), bringing larger specific humidity north

of the Alps (1 g kg^{-1}) and higher CAPE values (100 J kg^{-1}). RCM, on the contrary simulates a wetter surface level over Italy and the Mediterranean Sea. Surface temperatures in RCM are up to 2 °C higher in RCM than in CPM. . This causes outbound long wave radiation to be larger in RCM compared to CPM over those areas (10 W m^{-2}).Our analysis emphasizes the improvements of CPM for heavy precipitation modelling and highlights the differences against RCM that should be considered when using COSMO-CLM climate simulations.

1 Introduction

Heavy precipitation events cause tremendous damages and casualties in central Europe (Alfieri et al., 2016; Khodayar et al., 2021; Ranasinghe et al., 2021). In a warming climate, the occurrence and intensity of such events is projected to increase as assessed in Chapter 8 of the Intergovernmental Panel on Climate Change (IPCC) and previous publications (Douville et al., 2021; Pichelli et al., 2021), due to the intensification of the hydrological cycle (Rajcack and Schär, 2013; Ban et al., 2018). Such events may occur both during winter and summer fostered by Deep Moist Convection (DMC), a large vertical transport of precipitating air masses (Emanuel; 1994). In winter, heavy precipitation typically occurs under strong synoptic forcing (Keil et al., 2020), caused by the large-scale advection of positive vorticity in cold upper-level layers (Holton, 2013). The associated synoptic patterns have been studied in past literature (e.g., Knippertz et al., 2003; Werner and Gerstengarbe, 2010; Stucki et al., 2012) referring a strong influence of northerly cut-off geopotential lows and elongated troughs as well as of the Atlantic zonal flow. In summer, DMC is often triggered by favourable local and mesoscale conditions close to the surface, including a warm and moist low-level and a triggering mechanism (Doswell, 1996). When these conditions coincide with the arrival of a mesoscale low-pressure system, highly damaging precipitation is likely to occur.

Understanding heavy precipitation processes, their variability and trends at decadal time scales is needed to provide better prevention and adaptation strategies. Considering modelling approaches, dynamical downscaling with Regional Climate Models (RCM) has proven to be a valuable tool towards this end (e.g., Jacob et al.,2013). Recently, the development of Convection-Permitting Models (CPMs) led to a step forward (Coppola et al., 2018; Prein et al., 2020; Lucas-Picher et al., 2021) since a parametrized description of deep convection is no longer needed. An explicit representation of convection is often applied for horizontal grid spacings lower than ca. 5 km. Also improved is the representation of the model's land type, use and elevation (Prein et al., 2015; Heim et al., 2020). These advancements led to improvements in representing the daily precipitation's diurnal cycle (Kendon et al., 2012; Berthou et al., 2018; Ban et al., 2021); its structure, intensity, frequency, and duration (Berthou et al., 2019; Berg et al., 2019); its sub-hourly rates (Meredith et al., 2020); and orographic triggering (Ban et al., 2018). These improvements are consistent over the main modelling regions worldwide. However, not all problems are solved, since CPMs have also shown relevant wet biases, inducing an overestimation of extreme intensities (Kendon et al., 2012). CPM uncertainties arise from shortcomings in the physical parameterizations, the coupling of the numerics and the physics-dynamics, deficiencies in the representation of the initial conditions and the lack of sufficient high-resolution observations for validation (Lucas-Picher et al., 2021).

Particularly relevant for the improvement of heavy precipitation in CPM is the better representation of DMC processes, especially when convection is triggered close to the surface (Bui et al., 2018). In fact, studies have shown that CPMs induce stronger updraughts that leads to stronger convection (Meredith et al., 2015a; Meredith et al., 2015b). This is also observed in Numerical Weather Prediction (NWP) simulations (Barthlott and Hoose, 2015; Panosetti et al., 2018). When convection occurs over an area of complex orography, the finer representation of the mountains in CPM increases the triggering of convection (Langhans et al., 2012; Vanden Broucke et al., 2018; Heim et al., 2018; Vergara-Temprado et al., 2020), leading to a better agreement with radar observations (Purr et al., 2019). Regarding other model variables, previous papers argued that CPM improve the simulation of surface temperature (Ban et al., 2014; Prein et al., 2015; Hackenbruch et al., 2016), due to a better representation of the orography, as well as the cloud coverage (Lucas-Picher et al., 2021). Regarding the soil-moisture-precipitation feedback, past work has shown that RCM tends to show a positive sign (Hohenegger et al., 2009; Leutwyler et al., 2021) whereas CPM can show both negative and positive signs at the sub-continental and continental spatial scales, respectively. The reason is that wetter soils induce more frequent precipitation at RCMs but more intense events in CPM (Leutwyler et al., 2021). CPM seem to better agree with observations as previous observations showed a negative sign of the feedback due to an increased sensible heat flux over drier soils, and mesoscale variability in soil moisture which intensifies afternoon convection (Taylor et al., 2012). Moisture biases also affect the development of heavy precipitation where a wet bias was found for established RCM models (Lin et al., 2018; Li et al., 2020), as well as in CPM simulations (Risanto et al., 2019; Bastin et al., 2019; Caldas-Alvarez and Khodayar, 2020; Li et al., 2020). However, how both RCM and CPM deal with the moisture wet bias still is an open question. Regarding atmospheric instability Li et al., (2020), found larger Convective Available Potential Energy (CAPE) during the afternoon in CPM, which was correctly converted to larger precipitation at the Tibetan Plateau. Finally, the scale dependency of other variables of interest for convective development such as Equivalent Potential Temperature at 850 hPa (θ_e^{850}), has been seldom investigated.

The model evaluated in this paper is the COnsortium for Small scale Modelling in Climate Mode (COSMO-CLM; Schättler et al., 2016, Rockel et al. 2008) which is especially suitable for studying differences between RCM and CPM due its flexibility for configuration in convection parametrized and convection permitting resolutions. COSMO-CLM is a well-established regional climate model used by research and applied-science institutions in Europe (Sørland et al., 2021) and hence there is interest in quantifying its skill in simulating heavy precipitation its associated processes in a CPM set-up.

One established technique to work with large data sets, such as decadal climate simulations is Principal Component Analysis (PCA). PCA is a powerful method to reduce the dimensionality of a set (Joliffe, 2022) and to extract the principal underlying features. One of its applications is the derivation of the leading spatial patterns of atmospheric fields during specific situations, e.g., heavy precipitation (Knippertz 2003, Seregina et al., 2020). Provided PCA, also calculates the correlation between the days of the set and the derived spatial pattens, it can be used to construct composite maps of relevant model variables associated with the respective spatial patterns of a specific model variable, e.g., precipitation. Although PCA has been used for these applications in the past, to our knowledge, it has not yet been applied to study model differences between RCM and CPM. In this work we will derive composites of relevant model variables and study differences between both modelling set-ups.

The aim of this work is to evaluate reanalysis-driven RCM (25 km) and CPM (3 km) decadal long simulations of the greater Alpine area in the period 2000-2015 and assess their differences in representing heavy precipitation and associated environments. This paper is organized as follows: in Sect. 2 we introduce the dataset and methods employed; in Sect. 3 we present the main synoptic weather types bringing heavy precipitation; in Sect. 4 we evaluate heavy precipitation intensity and occurrence in the decadal simulations; in Sect. 5 we validate precipitation, humidity, and temperature fields of selected heavy precipitation events; in Sect. 6 we introduce the spatial patterns of precipitation derived from PCA, In Sect. 7 we present the differences of model variable composites and in Sect. 8 we provide our conclusions.

2.1 Observational datasets

We use observations from various sources for validation and comparison of the climate simulations (Tab. 1). We employ the Ensembles OBSservations (EOBS) gridded precipitation and relative humidity at the surface ($hurs$) products at 25 km resolution (EOBS-25km), which are provided by the European Climate Assessment & Dataset (ECAD) centre at 0.25° (ca. 25 km) of spatial resolution for the period 1950-2020. We use v.22.0e (Dec 2020) employing a 100-member ensemble created through stochastic simulations based on interpolated station data from national institutions including nine thousand rain gauges (Cornes et al., 2018). EOBS-25km has been widely used in previous literature for validation purposes (e.g., Tramblay et al., 2019; Bandhauer et al., 2021) and has been shown to have low median absolute biases with respect to other regional European precipitation products such as CARPATCLIM or Spain02 (Cornes et al., 2018).

The HYdrologische RASterdatensaetze (HYRAS) gridded precipitation dataset, provided by the German Weather Service (DWD) is available at 1 km (ca. 0.01°), 5 km (ca. 0.05°) and daily resolution. HYRAS covers Germany and neighbouring catchments in parts of Switzerland, Austria, the Netherlands, France, Belgium, and Poland (Fig. 1). The version v2 covers the period 1951-2015 and was derived using multiple linear regression and inverse distance weighting interpolation of 6200 rain gauges considering the orography (Rauthe et al., 2013, Razafimaharo et al., 2020). HYRAS-5km has a remarkable quality and its high-resolution enables a good representation of local scale features, outperforming the coarse resolution of EOBS-25km (Hu et al., 2020). However, it is only available over Germany and nearby catchments.

The Multi-Source Weighted-Ensemble Precipitation (MSWEP) is a gridded precipitation product provided by GloH2O (http://www.gloh2o.org/) at 0.1° (ca. 11 km) spatial resolution and 3-hourly temporal resolution for the period 1979-2020 with global coverage. We use version v.2.2.0. which was obtained through weighted interpolation of different observations to a common grid. It merges data from rain Gauge observations from Climate Prediction Center (CPC) unified and Global

Precipitation Climatology Centre (GPCC), satellite observations from the CPC MORPHing product (CMORPH), Global Satellite Mapping Precipitation Moving Vector with Kalman (GSMaP-MVK) and Tropical Rainfall Measuring Mission Multi-Satellite Precipitation Analysis (TMPA) 3B42, as well as two reanalyses' datasets ERA-interim and Japanese Reanalyses JRA-55 (Beck et a., 2019). MSWEP has a higher median correlation (up to 0.67) against stations, compared to CMORPH (0.44) and TMPA-3B42 (0.59) (Beck et al., 2017). We use the MSWEP product to profit from its high accuracy, shown in previous studies, globally (Beck et al., 2017, 2019; Xiang et al., 2021) as well as in specific geographies (Du et al., 2022; Peña-Guerrero et al., 2022). MSWEP has the advantage of covering sea surfaces and is adequate for precipitation event evaluation because it includes gauge data from CPC and GPCC.

The radiosonde data archived by the University of Wyoming (UWYO) are used to validate the RCM and CPM humidity and temperature profiles. The stations are located close to large European cities, with an average distance of 250 km between stations. The temporal resolution ranges between 6 h, 12 h and 24 h and the provided information includes height, atmospheric pressure, temperature, and dew point temperature on ca. 30 levels. The UWYO soundings have often been used as reference for validation studies (e.g., Ciesileski et al., 2014; Yang et al., 2020).

2.2 Setup of the COSMO-CLM, RCM and CPM simulations

We use COSMO-CLM, a non-hydrostatic model using the fully compressible atmospheric equations (Schättler et al., 2016), incorporating sub-grid turbulence, convection and grid scale clouds and precipitation parameterizations. COSMO-CLM uses a soil model called TERRA-ML (Doms et al., 2011) to parametrize the mass and heat exchanges between the surface and the atmosphere (Rockel et al., 2008).

In this work, we systematically compare reanalysis driven regional climate simulations with a typical RCM resolution (25 km; hereafter named RCM) and at convection permitting resolution (~ 3 km, named CPM). All simulations were performed with the version COSMO-CLM5 and use a setup specifically optimized for these resolutions.

The RCM simulation covers the period 1961-2018 (Tab.2), has a grid spacing of 0.22° (ca. 25 km), a 3-hourly output, and was performed within the scope of the MiKliP project (Feldmann et al., 2019). This simulation was performed for the Euro-CORDEX domain (Jacob et al., 2014) and thus covers the European continent and vast areas of the North Atlantic and the Mediterranean (Fig. 1). The RCM simulation is forced by ERA-interim (Dee et al., 2011) for the period investigated in this manuscript (2000-2015). The setup is the recommended for COSMO-CLM5 for typical RCM resolutions (10-50 km). The most relevant model settings are summarized in Tab. 2 and in Sørland et al., 2021.

The CPM simulation uses a COSMO-CLM5 subversion with a few bug-fixes and additional output variables but no changes in the numerics or formulation of the physics. The setup has been optimized for convection permitting scales and is used in the CORDEX Flagship Pilot Study on Convection (Coppola et al., 2018) and the simulation has been evaluated in Ban et al. (2021). This means that there are differences in the specific tuning parameters, where the main difference is the switching of the deep-convection parametrization (Tiedtke; 1989; Baldauf et al.; 2011; cf. Tab. 2). The simulation is performed by downscaling the RCM simulation described above over the grater Alpine area (ALP-3 domain, with a 3km (0.0275°) resolution for the period 2000 – 2015.

Another convection-permitting simulation – here called KLIWA-2.8km (cf. Tab. 2) – is used auxiliary just in Sect. 4 (Fig. 6) to extend the period for the comparison of the historical events. The grid spacing of this simulation is 2.8km (0.025°) and covers a smaller modelling domain over southern Germany and the Alps (cf. Fig. 1) for the period 1971-2000. It is forced by ERA40 re-analysis (Uppala et al., 2005) in a three-step nesting approach (Hundhausen et al., 2022). This simulation uses a slightly older subversion missing a few bug fixes. The main differences to CPM can be found in Tab. 2.

Two areas are investigated in our study. The first, denominated southern Germany (SGer, Fig. 1) encompasses the northern Alps, and southern Germany up to North-Rhein-Westphalia and Saxony. This area is selected to fulfil the requirements of the modelling and observational data sets (availability, coverage, time span). The second area, CPM (Fig. 1), covers the greater Alpine domain including the northern Mediterranean basin and is used for comparison of the model performance RCM vs. CPM.

2.3 Analytical methods

2.3.1 The Precipitation Severity Index (PSI)

We re-adapted the PSI, an index previously used to detect heavy precipitation events (Piper et al., 2016) and severe windstorms (Leckebusch et al., 2008; Pinto et al., 2012) to include precipitation persistence. By doing so we can consider three different, but intertwined aspects of heavy precipitation: grid-point intensity, spatial extent of affected area and temporal persistence. It is re-defined as follows:

$$PSI_T = \frac{1}{(1+d)\cdot A} \sum_{i=1}^{N} \sum_{j=1}^{M} \sum_{t=T-d}^{T} \frac{RR_{ijt}}{RR_{perc_{ij}}} \cdot (\Delta x)^2 \cdot \prod_{\tau=t}^{T} I\left(RR_{ij\tau}, RR_{perc_{ij}}\right) \qquad [1]$$

$$I\left(RR_{ij\tau}, RR_{perc_{ij}}\right) = \begin{cases} 0 \; if \; RR_{ij\tau} \leq RR_{80_{ij}} \\ 1 \; if \; RR_{ij\tau} > RR_{80_{ij}} \end{cases}$$

The PSI values at a certain time step T (PSI_T) are obtained from the ratio between grid point daily precipitation (RR_{ijt}) and a user-defined threshold. In this paper we set this threshold to be the 80-percentile ($RR_{perc_{ij}}$) all-day to neglect grid points whose precipitation is lower than the set threshold one for day T ($RR_{ij\tau} \leq RR_{perc_{ij}}$). This is done by means of the function $I\left(RR_{ij\tau}, RR_{perc_{ij}}\right)$. We consider the spatial extent by summing the ratios over the spatial extent (NxM) of the study region along the directions i and j. The ratios are multiplied by the area of one grid cell $(\Delta x)^2$. The precipitation persistence is considered in the calculation through the sum over time (t). The ratios at each grid point for day T and the previous d days ($d = 2$ in our case) are added for the PSI calculation, provided precipitation was continuous and larger than $RR_{perc_{ij}}$ at that same grid point i, j.. The daily PSI value is normalized to the area of the simulation domain $A = N \cdot M \cdot (\Delta x)^2$ multiplied by $(1 + d)$ to consider the addition of grid points with persistent precipitation. Prior to the PSI calculation, we include a correction for latitude stretching of the grid as $sqrt(cos(lat))$ following (North et al., 1982).

To assess the performance of the PSI, we calculate Spearman's rank correlations between the PSI and a simpler field sum index ($fldsum$). We use daily precipitation data from HYRAS-5km between 01-Jan-1971 and 31-Dec-2015 over the investigation area SGer (Fig. 1). We evaluate different combinations of the PSI parameters $RR_{perc_{ij}}$ and d (Eq. 1). Fig. 2 shows the rank correlations against $fldsum$ and the three top-ranked events of each implementation and the daily precipitation of the 22-Oct-1986 event.

We find a high rank correlation between the PSI and $fldsum$ for low values of $RR_{perc_{ij}}$ and d. For instance, when we set $RR_{perc_{ij}}$ as the percentile-80 of the 1971-2015 period and $d = 0$ (equivalent to considering no persistent precipitation) the rank correlation is 0.97, indicative of a very similar functionality between the PSI and $fldsum$ (Fig. 2a). For instance, in this configuration the third event in the ranking differs between the PSI (20-Dec-1993) and $fldsum$ (20-Nov-2015). The reason behind is that the 20-Dec-1993 event occurred over a flat area, unfrequently affected by heavy precipitation (Fig. S1 in the Supplementary Material; SM). The PSI ranks this event to 20-Nov-2015 (affecting complex terrain) because the threshold set to the 80-percentile is lower over flat terrain and thus easier to surpass (Fig. S1).

As we increase $RR_{perc_{ij}}$ and d, the rank correlation decreases, implying a different ranking of the events (Fig. 2a). For example, a percentile-95 for $RR_{perc_{ij}}$ and $d = 2$ brings a rank correlation of 0.86 which favours the detection of events with larger grid-point intensity and temporal persistence. For illustration, the 22-Oct-1986 event (Fig. 2b, c, d) is ranked as the most severe event in the period in this configuration due to precipitation totals between 50 mm d^{-1} and 150 mm d^{-1} impacting for three consecutive days the same areas, e.g., the Colmar region or the Marburg-Siegen area (see Fig. 2, b, c, and d). The remainder events can be seen in the SM.

To conclude, the advantage of the PSI with respect to a simpler field sum index is its capability to detect rarer and more persistent events. Rarer events can be found because the threshold $RR_{perc_{ij}}$ guarantees the selection of events where either heavy precipitation falls over climatologically drier areas or where extreme intensities take place over typically wet areas (e.g., complex terrain). For its part $d = 2$ favours the detection of events where heavy precipitation occurred continuously on the same grid point up to a maximum of wo days. That said, a low percentile threshold ($RR_{perc_{ij}}$) or $d = 0$ will bring a functionality no different to $fldsum$. This makes the PSI a flexible solution that can be tailored to the user´s needs. Finally, the PSI is also flexible to set the threshold $RR_{perc_{ij}}$ to a fixed amount, e.g., 120 mm d^{-1}, to ensure that only grid points above that threshold will be included in the calculation. This is a configuration that could be used in future studies.

2.3.2 Principal Component Analysis

Principal Component Analysis (PCA) is a method to reduce the dimensionality of a data set, by transforming it to a new coordinate system of variables called Principal Components (PCs; Joliffe, 2002). The functions that allow the transformation from the original set to the PCs space are called Empirical Orthogonal Functions (EOFs). The transformation is performed in such a way that the explained variance is concentrated in a small number of components. By construction, the leading EOF1 has the largest explained variance, followed by EOF2, and so on. In this paper, we investigate the PCs and EOFs of 500 hPa geopotential height fields (Sect. 3) and daily precipitation (Sect. 6). Similarly to Ulbrich et al., (1999), we obtain EOFs representing the spatial patterns of the target variable, that account for the main modes of variance. On the other hand, the PCs are time series which provide the information of the correlation of each EOF to a specific day in the series.

Given that the explained variance is now concentrated in a small number of variables, it is important to discern how many EOFs should be retained. With this aim, we use a method of parallel analysis based on the randomization of eigenvalues named the random-λ rule (Peres-Neto, 2005). The procedure is as follows, 1) a random data array is created with the same dimensions as the data array under study, 2) PCA is applied on the random array, 3) steps 1 and 2 are repeated up to 1000 times, retaining the eigenvalues showing a significance over 95 % (alpha= 0.05). 4). If the original eigenvalues exceed the critical values from the random data, then we reject the null-hypothesis (Peres-Neto, 2005). The random-λ rule is more suitable than other methods of parallel analysis such as the N-rule (Preisendorfer and Mobley, 1988) since it does not assume a normal distribution for the array of random values and thus works better for variables such as precipitation.

2.3.3 Validation metric Fractions Skill Score

The Fractions Skill Score (FSS) provides an estimation of the model's skill in representing the fraction of surface affected (or not) by heavy precipitation (Skok and Roberts, 2016). A perfect forecast has thus an FSS of 1. A simulation with no skill has an FSS of 0. In this work, we set a threshold of 40 mm d^{-1} to define structures affected by heavy precipitation. The threshold is in the range of values implemented by Roberts and Lean (2008) for simulations of spring convective rain over southern England. We select this threshold to be able to identify clear precipitation structures otherwise masked by the choice of a too large or too low threshold analogously to Caldas-Alvarez et al., (2021). Equation 2 defines the FSS following Roberts and Lean (2008).

$$FSS = 1 - \frac{\frac{1}{M}\sum_{i=1}^{M}(f_{mod}-f_{obs})^2}{\frac{1}{M}(\sum_{i=1}^{M} f_{mod}^2+\sum_{i=1}^{M} f_{obs}^2)} \qquad [2]$$

The fractions of surface affected by heavy precipitation are represented by f_{obs} and f_{mod}, for the observations and the model, respectively. Both are calculated as the number of grid points affected by precipitation over the defined threshold (40 mm d^{-1}) divided by the total number of grid points of a domain. FSS is computed as the ratio of the sums of fraction differences for M sub-boxes within the investigation domain. These M sub boxes are defined as sub-domains around M grid points with N near neighbours. N in our case is twelve since most of the events we validate have shown a skill larger than the target skill defined as $FSS_{target} = 0.5 + f_{obs}/2$ for $N = 12$. For detailed explanation, refer to Roberts and Lean (2008), Skok et al., (2016), and Caldas-Alvarez et al., (2021).

3 Synoptic weather types

We obtain the predominant large-scale situations associated with heavy precipitation applying PCA. We analyse the EOFs of geopotential height at 500 hPa, based on the RCM simulation, for the period 1971-2015. We select dates of heavy precipitation in the 98-percentile of severity (PSI) in the HYRAS-5km "all-day" data set over the investigation region SGer (Fig. 1). Figures 3 and 4 provide, respectively, the dominating weather types of heavy precipitation for summer (MAMJJA) and winter (SONDJF). The comparison against the CPM is not shown here since only negligible differences exist with respect to RCM, since the boundary conditions from the forcing reanalyses (ERA) strongly determine the large-scale features (Prein et al., 2015).

In winter, four synoptic patterns of 500 hPa geopotential height suffice to explain the majority of HP events, following the random-λ rule with a 95% significance in the t-test (Peres-Neto et al., 2005). They account for 74% of the heavy precipitation episodes. The first mode, representing 29 % of the events, is characterized by wave trains of low pressure associated with northerly incursions of polar air (Fig. 3). The synoptical situation is analogue to the Stationary Fronts (STF) category proposed by Stucki et al., (2012). In this situation, heavy precipitation over the Alps is associated with strong upper-level lifting over northern Italy and large south-westerly advection of moisture from the Mediterranean. Historical cases belonging to this category, as identified by the PCA, are the second phase of the 23-31 October storms in 1998 (Fuchs et al., 1998) or the late November events in 2015 (Tab. 3, https://www.wetter.de/cms/so-war-das-wetter-im-november-2015-2566771.html), for instance. The second mode, accounting for 22 % of the events, shows strong north-south gradients of the 500 hPa height and fast zonal circulations (Fig. 3). This synoptic pattern has been identified as a Zonal Flow (ZOW; Stucki et al., 2012) or as a narrow and elongated streamer (Massacand et al., 1998). The zonal circulation favours moisture advection from the Atlantic and can produce large precipitation in non-convective environments (Stucki et al., 2012). The 29 December 2001 event belongs to this precipitation mode, for instance. The third and four modes account for 12 % and 11 % of precipitation episodes, respectively and show similarities with the 500 hPa geopotential heights of the second mode (Fig. 3). However, the third synoptic pattern shows a weaker Azores high, favouring the advection of Atlantic moisture with a south-westerly component. The fourth mode, for its part, shows a weaker polar low, which favours the development of anti-cyclonic circulation (Fig. 3) .

In summer, five synoptic patterns of 500 hPa geopotential height are discernible from random noise (Peres-Neto et al., 2005), accounting for 77 % of the events. The first mode, corresponding to 27% of the considered dates, shows an extended upper-level trough from the British Isles down to southern France (Fig. 4). This configuration shows elements of an Elongated Cut-Off (ECO) and of CAnarian Troughs (CAT; Stucki et al., (2012). In such situations upper-level lifting occurs east of the trough together with southerly moisture advection either from the southwest or the southeast, respectively. Such situation occurred for instance during the first stages of the large central European flooding of early June 2013 (Kelemen et al., 2016). If a blocking situation occurs, for instance Omega blocking, the persistence of precipitation is enhanced and can lead to recurrent events (Kautz et al., 2021) at the eastern flank of the ECO or CAT. The second summer precipitation mode (Fig. 4), accounting for 19% of the events, presents a similar pattern to the third and four modes of winter precipitation (Fig. 3) with the characteristic strong zonal flow from the Atlantic. Examples of this synoptic configuration are the March 1988 events flooding the Rhein river (southern western Germany; Prellberg and Fell, 1989) or the 15 June 2007 events affecting southern Germany (https://www.wetteronline.de/extremwetter/schwere-gewitter-und-starkregen-schaeden-durch-tief-quintus-2007-06-15-tq). The third precipitation mode, explaining 12 % of the analysed days (Fig. 4), shows similarly to the first mode, an ECO, however, with an eastward shifting of the Azores ridge and the possibility of evolving to a Pivoting Cut-Off Low (PCO; Stucki et al., 2012). If the PCO finally realizes and reaches the Mediterranean it is accompanied by a cyclonic flow, which advects moisture towards Central Europe, which originates in the Balkan region. This has been demonstrated to be the case for the second phase of the June 2013 flooding (Kelemen et al., 2016). The fourth summer precipitation mode (Fig. 4), accounts for 11% of the considered episodes and represents situations of north-easterly development of the upper-level trough. The low pressure evolves into a CAT situation inducing a south-westerly moist inflow to the Alpine region (Stucki et al., 2012). The 08 July 2004 floods in Baden-Wuerttemberg (southwestern Germany; http://contourmap.internet-box.ch/app/okerbernhard/presse2.htm) are a good example of such situation. The fifth precipitation mode, 8 % of the events, shows an STF pattern, similarly to the first winter precipitation mode (Fig. 3). Such a configuration was present during the Rhein-Necker flooding (western Germany) in June 2005 (https://www.rnz.de/nachrichten/metropolregion_artikel,-unwetter-folgen-in-mannheim-besonders-viele-gebaeudeschaeden-durch-regen-_arid,482078.html).

4 Evaluation of heavy precipitation

After identifying the synoptic situations responsible for heavy precipitation, we evaluate the RCM and CPM simulations between 2000 and 2015 (Tab. 2) in terms of probability, intensity, and detection capability against observations.

Figure 5 shows empirical Probability Distribution Functions (PDFs) of daily precipitation between 1971 and 2015 over SGer (Fig. 1). All datasets represent similar probabilities for precipitation intensities between 0 mm d^{-1} and 50 mm d^{-1}. The upper box in Fig. 5 shows a zoom-in for the lower intensities. Beyond 50 mm d^{-1} CPM (red) starts to diverge from RCM (blue) and the observations (HYRAS-5km in black and EOBS-25km in grey). CPM (red) can represent daily grid point intensity up to

280 mm d^{-1}, whereas RCM (blue) can only attain 150 mm d^{-1}. HYRAS-5km, for its part, reaches a maximum grid point intensity of 215 mm d^{-1} and E-OBS-25km reaches 180 mm d^{-1} This shows that the coarser resolution data sets represent lower precipitation intensities and that CPM shows the largest probabilities of representing heavy precipitation intensities (>120 mm d^{-1}).

The ability of CPM to represent larger precipitation rates agrees with previous literature (Ban et al., 2014; Prein et al., 2015; Fosser et al., 2014), which has been related to the enhanced intensities over orographic terrain (Langhans et al., 2012; Vanden Broucke et al., 2018; Ban et al., 2021). The comparison against HYRAS-5km (black), shows a good agreement by RCM and CPM for values between 1 mm d^{-1} and 50 mm d^{-1}. However, CPM (red) overestimates heavy precipitation for grid point maxima. This is a well-known deficit (Kendon et al., 2012; Berthou et al., 2018). It should also be noted that even for grid resolutions down to 1 km the updrafts might not me simulated with the right intensity, which can help explain the overestimation of precipitation at these high resolutions (Vergara-Temprado et al., 2020). It is also worth noting that the comparison against observations can suffer from under catchment viewpoint, as the misplacement of the heavy precipitation can lead to strong local reductions, reaching even 58 % in the worst scenarios (Vergara-Temprado et al., 2020). Furthermore, problems associated with the gridding of precipitation observations and the fact that rain-gauges in the Alpine region tend to be located at the valleys, add uncertainty to the estimation of precipitation.

To further assess the performance of COSMO-CLM in representing precipitation extremes we analyse the detection capability of RCM and CPM by means of a dot diagram, showing the 500 most severe events detected with the PSI in the period 1971-2015 over SGer in Fig. 6. The CPM dataset is extended to 1971 with the aid of the KLIWA-2.8km simulation that has a similar horizontal resolution (2.8 km) and is obtained using the same model (CCLM). However, inconsistencies exist between CPM and KLIWA-2.8 (refer to Sect. 2.2 for further details). We use HYRAS-5km (black circles and EOBS-25km (grey squares) as reference.

CPM (red dots) showed a higher spearman’s rank correlation (0.48) than RCM (blue circles; 0.41) as shown in the legend of Fig. 6. Likewise, CPM outperforms RCM with regards to hit rate (number of hits divided by number of occurrences) with values of 47.2 % for CPM and 45.88 % for RCM (not shown). The rank correlations of both resolutions remain below 0.5 given the difficulty of exactly represent the same 500 events in a 44-year climatology representing 3% of all considered days. Figure 6 also allows observing relevant periods of heavy precipitation clustering, e.g., spring-summer of 1971, winter 1989, the years 2000 to 2002 and autumn 2013. Finally, EOBS-25km (grey squares), has a rank correlation of 0.94 against HYRAS-5m indicating a good accuracy for this product.

5 Event scale evaluation

In the previous section, we assessed an overestimation of grid-point heavy precipitation for the convection-permitting simulation CPM, but a reliable performance in detecting severe precipitation events in a 44-year climatology. Here we evaluate the performance of CPM at the event scale validating eight events. We focus on the period 2000-2015 and the investigation area CPM (Fig. 1).

Table 3 shows eight events selected using the PSI, which were also included in the derivation of the synoptic weather types in Sect. 3. Table 3 provides information about the duration of the events, the observed total precipitation, maximum grid point intensities, percentage of affected area (percentage of grid points with precipitation over the 80th percentile), severity (PSI), and associated Weather Types (WT). We subjectively shortlisted the events to consider not only those events with large severity (PSI) and but also to have sufficient winter and summer cases, which led to the consideration of two events with daily totals below 120 mm d^{-1}, namely 03-Nov-2002 and 08-Jul-2014.

5.1 Precipitation

We focus on two aspects of heavy precipitation, (1) amount, calculated as aggregated precipitation in time and space, and (2) structure, validated by means of the FSS metric (Sect. 2.3.3). For both metrics, we use MSWEP-11km (Tab. 1) as the observational reference, after coarse-graining all compared datasets to a common grid of 25 km. MSWEP-11km is used provided its large accuracy due to the inclusion of rain gauges (Beck et al., 2017) and since precipitation occurs to a large extent over the Mediterranean Sea, where HYRAS-5km and EOBS-25km have no coverage.

Table 4 shows the relative differences in precipitation amount aggregated in space and time between the model and observations as $RR_{rel.diff} = (MOD - OBS)/OBS$. CPM performed better than RCM in six out of the eight selected cases for precipitation amount. The largest improvement occurred for the 31-May-2013 event, which corresponds to the synoptic pattern S1 associated with the occurrence of ECOs and the advection of south-westerly moisture (Fig. 4). Using CPM brought larger precipitation rates, in agreement with the findings of Sect. 4, allowing for better scores of aggregated precipitations.

Regarding structure, CPM performed well in7 out of 8 events with FSS reaching values over 0.7. RCM, for its part, performed well for 5 out of 8 events (Tab. 4). The 31-May-2013 event is again an example of good performance by CPM, where the FSS scores reached 0.87 in CPM (0.26 in RCM). The main reason for this improvement was the ability of CPM to represent larger precipitation structures over the Alps in a better agreement with MSWEP-11km. The spatial distributions of precipitation by RCM, CPM and MSWEP-11km are shown in Fig. S2 of the SM.

Only the event 08-Aug-2007 showed a deficient performance by CPM, both for precipitation amount and structure. This event occurred under a S1 synoptic situation associated with an elongated troughs or cut-off lows (Fig. 4). The reason behind is the large underestimation of precipitation in CPM, which also hampers the structure representation.

Overall, these results showed that CPM outperforms RCM in the representation of precipitation amount and structure. The advantage of CPM lies on the better location of orographic precipitation and the larger precipitation intensities.

5.2 Humidity and temperature

In addition to precipitation errors, temperature and humidity biases could affect our interpretation of the model differences between RCM and CPM. To reduce uncertainty, we validate specific humidity (hus) and temperature (ta) profiles from RCM and CPM against radiosondes from the University of Wyoming (UWYO) and surface relative humidity ($hurs$) against EOBS-25km for the eight selected events (cf. Tab. 3).

Figure 7 shows the temporal Mean Bias (MB; thick line), the standard deviation of the differences (shaded area), and the Root Mean Square Errors (RMSE; dashed line) of specific humidity (Fig. 7a) and temperature (Fig.7b). The model output is interpolated to the location of eleven sounding stations, which were selected to have sufficient availability and fulfil the condition of a surface height difference not larger than 50 m. This requirement is introduced to avoid including large humidity and temperature biases from differences in surface topography between the model and the observations. We include all available soundings during the duration of the eight events (Tab. 3) in the calculation, with a temporal resolution between 6 h and 12 h.

Humidity is slightly overestimated by RCM throughout the whole profile and by CPM above 800 hPa (Fig. 7a). The overestimation by both models reaches 0.2 g kg^{-1} at 700 hPa. Below 800 hPa, CPM, reduces the mean bias reaching -0.1 g kg^{-1}, indicating a generally drier planetary boundary layer. RMSE values are similar for both simulations being close to 1.5 g kg^{-1} below 700 hPa. These results are promising for COSMO-CLM since RCM and CPM show small biases even if they do not have an active data assimilation scheme and whence the model is exclusively constrained by the boundary conditions of the forcing data (ERA-interim).

Regarding temperature (Fig. 7b), COSMO-CLM shows a warm bias, reaching 0.5°C at the 925 hPa layer for both resolutions. RMSE (Fig. 7b, dashed line) is remarkably similar between both simulations, above 2 °C, with a slight improvement by CPM (red).

The humidity (Fig. 7.c) and temperature (Fig. 7.d) profiles show a wetter mid-troposphere (between 700 hPa and 925 hPa) in RCM than in CPM and a similar temperature profile between both simulations with a good agreement against observations. CPM simulates slightly better the vertical humidity profile than RCM with a steeper humidity-height gradient. This was also observed in earlier studies with COSMO and COSMO-CLM (Caldas-Alvarez and Khodayar, 2020; Caldas-Alvarez et al., 2021). COSMO-CLM compensates the modelling errors simulating a wetter lower troposphere in RCM to help activate the deep convection parameterization scheme (Tiedtke, 1989). Being of the low-level control type, the Tiedtke deep convection scheme requires a sufficient moisture amount below the cloud base to initiate convection (Doms et al., 2011). By doing so RCM simulates precipitation totals of the same order as CPM that relies more upon the intensification of vertical wind speeds. Furthermore, the higher humidity in the mid-troposphere helps reduce the simulated dry-air entrainment increasing the total simulated precipitation. Both simulations show a reliable performance considering the decadal timescales

Provided the observations available below 925 hPa in the UWYO soundings were scarce, we employ the gridded EOBS-25km dataset (Tab. 1) to investigate the COSMO-CLM biases at the surface (Fig. 8). We represent the spatial distribution of temporal mean bias (colour shading) and the temporally-spatially averaged mean bias and RMSE of daily surface relative humidity. We calculate relative humidity biases for this validation, given no surface specific humidity gridded observations with sufficient accuracy were available for our region and period of investigation.

COSMO-CLM underestimates surface relative humidity for both RCM (Fig. 8a) and CPM (Fig. 8b), which is consistent with the well-known dry and hot bias of CPMs, provided our selected events occur mostly in summer. This is especially so at the Po Valley (Italy) and the southern Italian Peninsula. However, CPM (Fig. 8b), slightly improves the surface relative humidity deficit at locations north of the Alps, e.g., north-western France, the Czech Republic and western Austria. These corrections in the north-western part of the simulation domain, reduce the temporal and spatial MB by 3%. However, provided the larger spatial variability of this variable in CPM, due to the better orography representation, the RMSE is worsened by 5 %.

The profile and surface humidity and temperature validation has shown that: a) COSMO-CLM performs well in simulating the humidity and temperature lapse-rates, albeit small biases up to 0.2 g kg^{-1} in humidity and 0.5 °C (warm bias) in temperature exist; b) CPM simulates slightly better the vertical humidity profile with a steeper gradient than RCM; c) CPM reduces the positive surface relative humidity bias over locations north of the Alps, e.g., western France, the Czech Republic and eastern Austria.

6 Main modes of heavy precipitation variability in RCM and CPM

To understand where RCM and CPM represent the main spatial patterns of heavy precipitation differently, we use PCA (Sect. 2.3.2) on events detected in HYRAS-5km in the period 2000-2015. We do this to observe differences in the spatial distributions of heavy precipitation during the most frequent precipitation modes and reduce the dimensionality of the data set. We combine the severe events into one set and apply PCA to obtain the EOFs and their corresponding spatial distributions. We do this separately for winter (SONDJF) and summer (MAMJJA) events for both RCM and CPM, using days above the percentile-90 of daily PSI values. In total, 290 events per season are considered to derive the EOF maps shown in Fig. 9 and in Fig. S3 in the SM. For this analysis, we focus exclusively on precipitation EOFs with a similar structure between RCM and CPM, dismissing the remainder EOFs. This is done to ensure we compare model differences in similarly simulated meteorological situations.

Figure 9 shows the four leading EOF maps for winter events (panels a, c, e, and g) and the three leading modes in summer (panels b, d, and f) as simulated by CPM. The corresponding figures for RCM can be found in the SM (Fig. S3). Only CPM is shown here due to the large similarity in the spatial distributions of these EOFs with RCM. The PCA determines that the precipitation EOFs start to differ substantially between RCM and CPM after the leading four EOFs in winter and the third in summer. The four leading EOFs in winter explain 48% of the variability for RCM and 47% for CPM, being the first mode the most frequent one (22% of cases). For summer events the three leading modes of precipitation stand for 37 % of the situations in RCM and 33 % in CPM).

The visual inspection of the first EOF for winter events (Fig. 9a) shows that this the mode associated with orographic precipitation over the Alps and the northern Apennines in the Genoa region. EOF-2 (Fig. 9c) for its part shows precipitation either affecting continental Europe, north of the Alps (negative mode; brown) or affecting the Mediterranean, including the Italian and Balkan peninsulas with a marked orographic signal (positive mode; green). EOF-3 (Fig. 9e) combines precipitation over northern Europe with Mediterranean precipitation in its positive mode (green). The negative mode (brown) affects the southern Mediterranean basin between Italy and France as well as the southern and Maritime Alps. Finally, EOF-4 (Fig. 9g) shows a positive mode associated with precipitation over the Gulf of Lyons, the Balearic Sea, and the Pyrenes (green), and a negative mode affecting northeastern Italy (brown). The latter situations of heavy precipitation in the Mediterranean have been studied in detail in the HyMeX project (Khodayar et al., 2021).

The first EOF for summer events (Fig. 9b) is associated with orographic precipitation over the Alpine region, similarly to winter EOF-1, albeit affecting parts of northern Europe, where convection can trigger more easily during the summer months. EOF-2 (Fig. 9d) shows a similar pattern to winter EOF-4 (Fig. 9g) and summer EOF-3 (Fig. 9f) shows a pattern similar to winter EOF-2 (Fig. 9c).

To summarize, RCM and CPM simulate similarly the main precipitation modes up to the fourth principal component in winter and the third in summer. These precipitation modes account for 47 % of the precipitation variability in winter and 37 % in summer, implying that the remainder precipitation variance shows remarkable differences between RCM and CPM.

7 Model differences between RCM and CPM using composites

To further analyse model differences between RCM and CPM, we derive composites of model variables from each EOF in Fig. 9. We focus on model variables influencing the simulation of heavy precipitation e.g., Integrated Water Vapour (IWV), CAPE, soil-atmosphere heat fluxes, etc. To derive the composites, we select the days where daily precipitation showed the largest resemblance to the positive and negative modes of the precipitation EOFs. In other words, we select the days showing the largest positive (negative) correlations to the positive and negative modes of each precipitation EOF. This is done separately for RCM and CPM selecting the days with positive and negative correlations larger than one standard deviation of the full set. This leads to composites of ca. 30 days per positive and negative mode. We then average in time the spatial distribution of the selected days and obtain maps of the differences between RCM and CPM as in Fig. 10. For heavy precipitation differences, we work with composites of the days assigned to each EOF, whereas for other model variables we use the day prior to heavy precipitation. This done to study the model differences in the pre-conditioning of the event.

7.1 Heavy precipitation

The composites show relevant differences in precipitation amount (up to 8.5 mm h^{-1} i.e., 204 mm d^{-1}) between RCM and CPM throughout the complete greater Alpine domain, irrespective of the simulation and meteorological situation. Spatially averaged, both RCM and CPM can represent larger precipitation than their counterpart, however, in summer, CPM represents larger precipitation at the mountain tops e.g., the Alps, the Apennines. This holds for all analysed EOFs and both positive and negative correlations of the principal components. For illustration, Fig. 10a shows the composite differences of the negative principal components of EOF-2 in winter. Differences up to 6 mm h^{-1} are located east of the Spanish coast (RCM, blue) over the Apennines (Italy) and over the eastern and the Dinaric Alps (CPM, red). Spatially averaged, RCM simulates larger precipitation (0.21 mm h^{-1}) for this EOF. Fig. 10b shows the positive principal components of EOF-3 in summer, where again, CPM simulates larger precipitation than RCM over the Apennines (Italy), the Dinaric Alps (Balkans), and to a lower extent over the western Alps (Switzerland) and the Central Massive (France). All remainder composites are included in the SM.

These results highlight that RCM and CPM can simulate comparable precipitation amounts in the timely averages of daily precipitation (for the investigated EOFs). Regarding the larger precipitation amounts simulated by CPM over the mountain ranges, a plausible explanation is the intensification of vertical winds observed in previous studies comparing horizontal resolutions (e.g., Langhans et al., 2012; Barthlott and Hoose, 2015; Vergara-Temprado et al., 2020). Another explanation is provided by Vergara-Temprado et al., (2020) addressing that the "increase in precipitation with resolution could be happening as smaller grid boxes are easier to reach saturation". However, the presented analysis does not allow splitting the contributions from resolution increase from other factors, e.g., changes in the physics or physical parameterizations (see Sect. 2.2).

7.2 Integrated Water Vapour (IWV) and Equivalent Potential Temperature at 850hPa (θ_e^{850})

Two variables typically regarded as precursors of heavy precipitation are IWV and θ_e^{850} (Doswell et al., 1996; Stucki et al., 2016). The differences of the composites show larger IWV in RCM compared to CPM throughout the whole greater Alpine region in all analysed EOFs. The IWV differences can be as large as 2 mm and take place especially over the Mediterranean Sea and the Po Valley. θ_e^{850} shows differences up to 4 K more in RCM compared to CPM. Atmospheric water vapour is the main precursor of the θ_e^{850} differences as RCM is wetter than CPM in the 850 hPa level (Fig. 7). For illustration Fig. 11 shows the composite differences of IWV (colour shading) and θ_e^{850} (contours) for the same principal components as Fig. 10. The composites show IWV differences up to 1 mm over the Mediterranean Sea and up to 2 K for θ_e^{850} (Fig. 11a). Likewise, the negative principal components of EOF-3 show IWV differences up to 3 mm over France and 3 K differences in θ_e^{850} by RCM (blue; Fig. 11b). The remainder composites can be found in the SM.

7.3 Soil-Atmosphere interactions

Regarding variables such as surface heat fluxes, surface humidity and temperature, CAPE and Outgoing Longwave Radiation (OLWR), we find that CPM simulates larger outbound latent heat emissions than RCM over land, but that RCM represents larger latent heat fluxes than CPM over the Sea (up to 15 W m^{-2}). These differences cause CPM to simulate larger near-surface specific humidity than RCM over land from northern Europe down to the Alpine barrier. South of the Alps and over the Mediterranean Sea, the opposite occurs, and RCM simulates generally wetter near-surface conditions with differences up to 1 g kg^{-1}. An example of these model responses is illustrated in Fig. 12 (panels a and c) for the positive principal components of summer EOF-2 (Fig. 9.d). Provided the larger surface specific humidity simulated in CPM, north of the Alps, CAPE is also larger compared to RCM due to its relationship between close-to-ground moisture (Fig. 12.e).

Analog to the latent heat, sensible heat fluxes show relevant differences, with RCM emitting up to 20 W m^{-2} more than CPM over land, especially in summer (Fig. 12.b). This causes surface temperature to be larger in RCM than in CPM (up to 1.3 ºC), although exceptions exist as is the case of the composites of summer EOF-2 shown in Fig. 9d. Finally, the temperature differences close to the surface influence OLWR, whereby RCM emits larger OLWR than CPM for most of the analysed modes and their corresponding composites Fig. 12.f is however an exception with CPM emitting larger OWLR. All composite plots can be found in the SM.

In general, the previous results hold both for summer and winter events. However, CPM emits larger latent heat flux than RCM over all land areas during winter. Also, it is worth noting that the surface temperature differences are weaker in the southern part of the domain, e.g., over Italy and the Po Valley where CPM can show higher surface temperature . These signals cannot be attributed to severe precipitation regimes exclusively as they were present in the seasonal means for IWV, surface temperature and humidity, and outbound latent and sensible heat flux (see Figs. S16 and S17 in the SM). Finally, we would like to emphasize that our analytical approach does not allow us to relate the soil-atmosphere differences between RCM and CPM with the observed precipitation differences of Sect. 7.1.

8 Conclusions

The recent advancements in Convection Permitting Modelling (CPM; horizontal resolution below ca. 4 km) have been of pivotal relevance for the understanding and simulating heavy precipitation, at decadal time scales. These events with high impact, are projected to be more intense and frequent in a warming climate. Therefore, despite the improvements already assessed, further research is needed to understand the implications of reaching CPM in the simulation of precipitation formation processes. In this study we evaluated reanalysis-driven COSMO-CLM simulations for the greater Alpine region over the 2000-2015 period and assessed the differences between a Regional Climate Model (RCM), set-up (grid-size 25 km), and a CPM set-up (grid-size 3 km). The main results are presented below:

- CPM represents larger precipitation intensities, a better rank correlation, better hit rates for extremes detection, and a better representation of precipitation amount and structure for selected heavy episodes than RCM. However, CPM overestimates the heaviest intensities compared to observations, (also observed in Kendon et al., 2012, and Berthou et al., 2018).

- The new implementation of the Precipitation Severity Index (PSI), including a persistence parameter, proved useful for event detection in decadal datasets. Its main advantages are its flexibility to account for precipitation persistence and to allow for definition of an intensity threshold. Including these two parameters favours the ranking of longer lasted and rarer events whereas setting them to zero leads to a normal spatial averaging of daily precipitation.

- Principal component analysis showed that winter heavy precipitation events during 1971-2015 in the greater Alpine area occur either under stationary front situations with polar low pressure descending to the mid-latitudes or under strong north-south gradients of the 500 hPa geopotential height with a zonal flow. Four principal weather types suffice to explain most of the natural variability of winter cases. summer events are associated to either frontal convection on the western sector of elongated upper-level troughs and evolved cut-off lows, or due to winter-like synoptic patterns of stationary fronts over central Europe or strong zonal flows. Five PCs are enough to explain the natural variability of summer cases.

- Principal component analysis revealed that the leading modes of the analysed heavy precipitation events start to differ between RCM and CPM after the fourth leading mode in winter (47% of cases) and the third leading mode in summer (33 % of cases). This implies that more than half of severe precipitation events are represented differently in RCM and CPM and thus the choice of modelling approach is crucial, especially for summer cases. Composite maps derived from the leading modes showed that CPM systematically represents more precipitation at the mountain tops, but that RCM may show large intensities (up to 200 mm d^{-1}) in other regions.

- RCM represents larger Integrated Water Vapour than CPM, especially over the Mediterranean Sea and the Italian Peninsula in the pre-conditioning of summer events (up to 2 mm). The larger moisture in RCM comes from an intensified latent heat flux emission over the Sea and a wetter lower free troposphere. This was validated for 8 selected reprecipitation events against radiosondes. As a result, Equivalent Potential Temperature at the 850 hPa level was also systematically larger in RCM than in CPM (up to 3 K).
- At the ground level, CPM simulates larger latent heat flux over land than RCM (up to 15 W m^{-2}) on the day prior to severe precipitation. This occurs both for summer and winter composites although in summer this effect is constrained to areas north of the Alps. Over the Sea, the opposite occurs, and RCM simulates larger heat fluxes compared to CPM

(30 W m^{-2}). The consequence is a wetter surface level (1 g kg^{-1} specific humidity) and larger CAPE (140 J Kg^{-1}) in CPM north of the Alps, and a wetter surface level in RCM over the Mediterranean Sea and Italy, possibly associated with the southerly Mediterranean winds. In turn, RCM simulates larger sensible heat fluxes over land which leads to a generally hotter surface level than in CPM (by about 1.5 °C). These differences are weaker to the south of the Po Valley. Finally, the higher temperatures over land in RCM bring larger emissions of outbound long wave radiation compared to CPM (9 W m^{-2}).

It is worth mentioning that for variables such as surface specific humidity and temperature, or surface heat fluxes, the signal of the differences between RCM and CPM was already present in the seasonal means (Fig. S16 and S17). This implies that they are not exclusive of heavy precipitation situations but that could be present in other weather regimes. For instance, the fact that CPM represents larger temperature at the Po Valley in the summer means adds on the findings by Sangelantoni et al., (2022) where an amplification of heat waves over the same area was found in a CPM ensemble .

Our study has limitations that need to be briefly addressed. First, we only assess one regional climate model and hence our results cannot be generalized to other RCMs. Second, as is common in heavy precipitation studies the under-catchment problem might be present in the observations used for validation (Groisman and Legates 1994; Golubev, 1986; Goodison et al., 1997; Vergarara-Temprado et al., 2020). Finally, we would like to point out that our study compares two different simulations where the differences observed are due to the use of a different horizontal resolution (25km vs 3km) but also to the different fine-tuning of the settings and the different boundary data.

Notwithstanding these limitations, our study provides evidence of the added value of CPM and of the remarkable differences existing between RCM and CPM. These systematic differences must be considered when using one set-up or the other in decadal simulations. This is relevant for future research in the field but also for third parties interested in using climate information at decadal time scales. Examples of endeavours where high-resolution climate data are bringing added value are, for instance, the downscaling of climate change projections (Pichelli et al., 2021), the development of decision-relevant strategies for Climate Change adaptation (BMBF-RegiKlim) or their use in forestry or hydrology applications.

9 Figures and tables

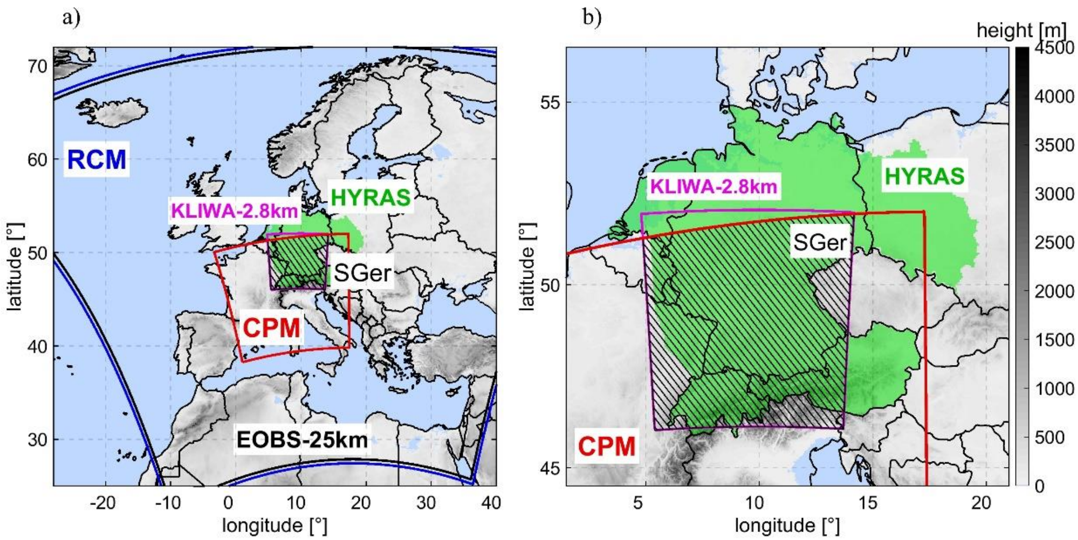

Figure 1. a) Simulation, and observation domains for RCM (25km; blue), CPM (3 km; red), KLIWA-2.8km (magenta); HYRAS-5km (green), and EOBS-25km (black). The two investigation domains of this study are Southern Germany (SGer; dashed box), and the CPM domain.

a)

	$fldsum$	PSI ($RR_{80_{ij}}$, d=0)	PSI ($RR_{80_{ij}}$, d=2)	PSI ($RR_{95_{ij}}$, d=2)
Rank Corr.	1.00	0.97	0.96	0.86
1	07-Aug-1978	07-Aug-1978	22-Oct-1986	22-Oct-1986
2	14-Feb-1990	14-Feb-1990	15-Feb-1990	14-Feb-1990
3	20-Nov-2015	20-Dec-1993	14-Feb-1990	20-Dec-1993

b) c) d)

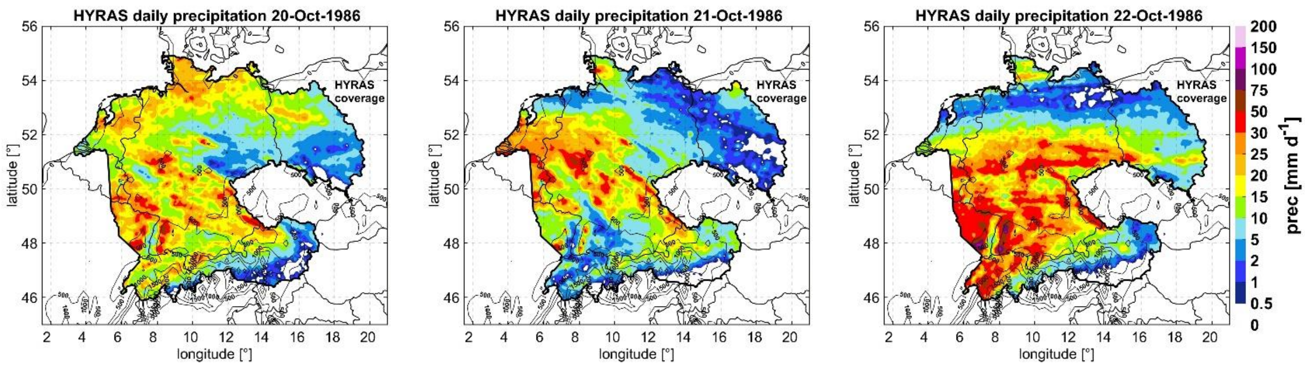

Figure 2. (a) Rank correlations between $fldsum$ and different configurations of the PSI daily values in the period 1971-2015 over SGer obtained with HYRAS-5km. The top three events of the period are shown for each index. (b), (c), and (d) show spatial distributions of daily precipitation measured by HYRAS-km on the 20, 21 and 22 October 1986.

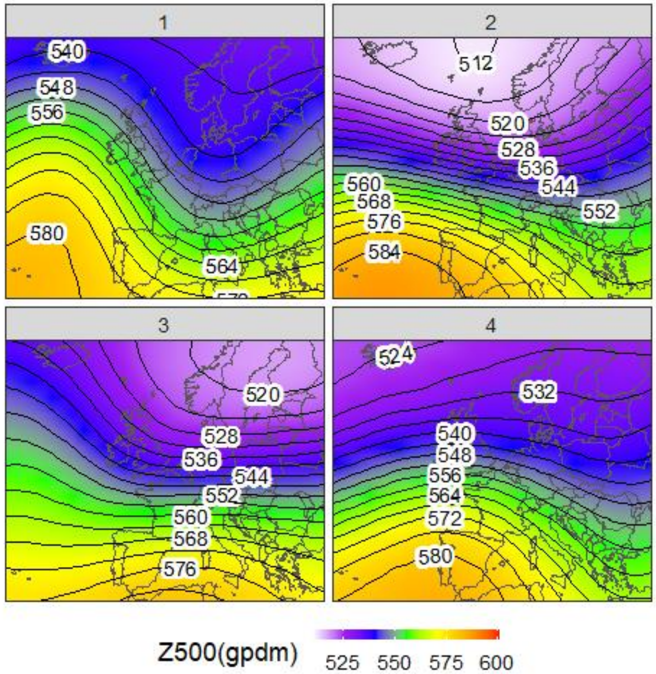

Figure 3. Synoptic weather patterns based on Principal Component Analyses for the 98-percentile most severe precipitation cases in region SGer in winter (SONDJF) of the 1971-2015 period, detected with the PSI. The spatial distributions show 500 hPa geopotential height in geopotential decametres (gpdm) obtained from RCM. The analysis has been performed with the SynoptReg R package (M. Lemus-Canovas et al., 2019).

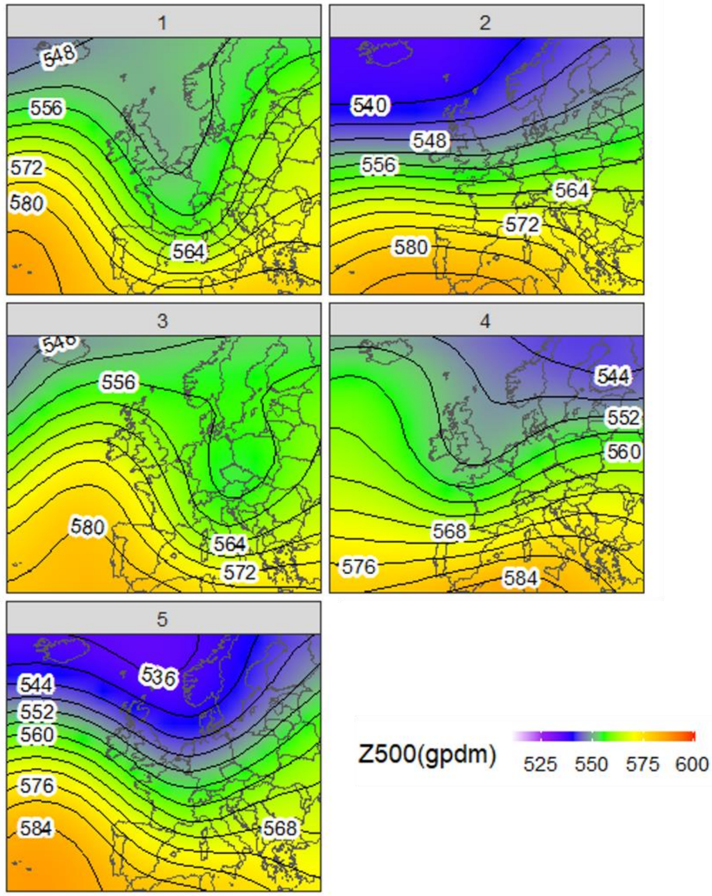

Figure 4. As Fig. 3 for summer extreme precipitation days (MAMJJA).

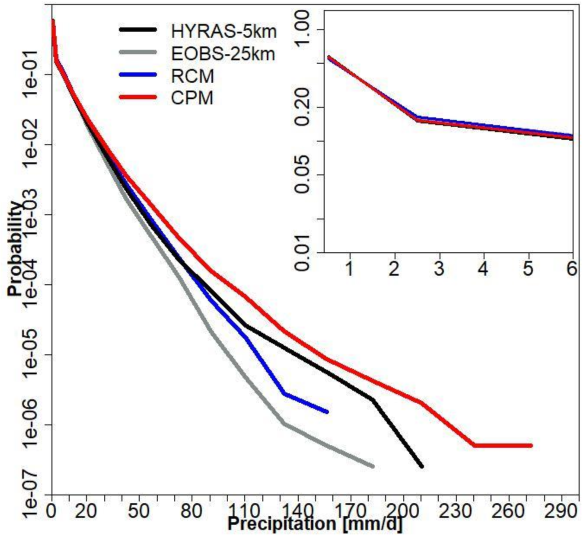

605 **Figure 5. Empirical Probability Distribution Functions (PDF) of daily precipitation over SGer in the period 2000-2015 from HYRAS-5km (black), EOBS-25km (grey), RCM (blue), CPM (red). The lowest precipitation rates are shown in the upper-right corner subpanel.**

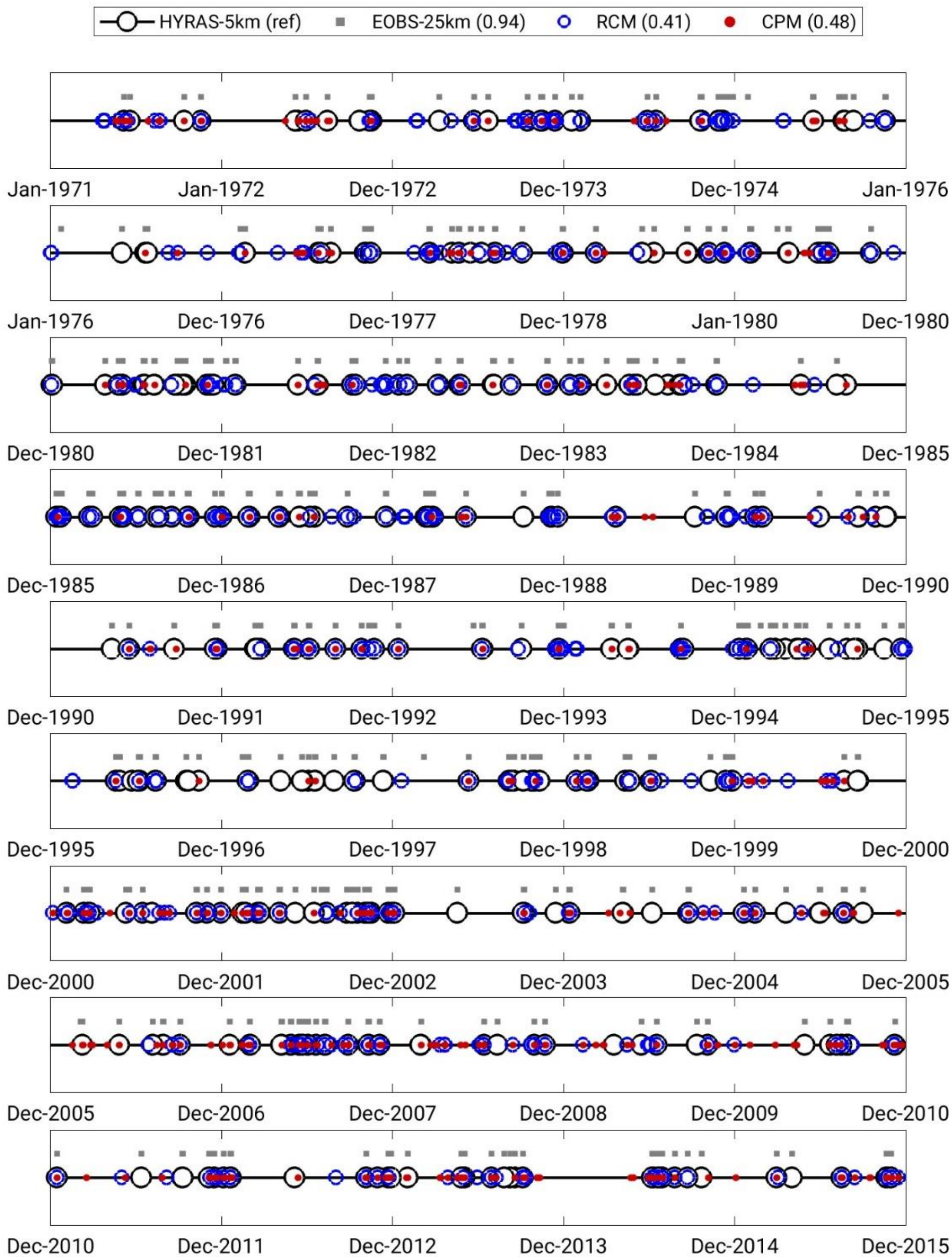

Figure 6. Dot diagram of the period 1971-2015, showing the 500 most severe precipitation events, detected using the PSI for HYRAS-5km (black circles), EOBS-25km (grey squares), RCM (blue circles), and CPM (red dots). The CPM data set is extended from Jan-1971 to Dec-1999 using KLIWA-2.8km (Sect. 2.2). The spearman's rank correlation of the data sets is shown in the legend where HYRAS-5km taken as the reference.

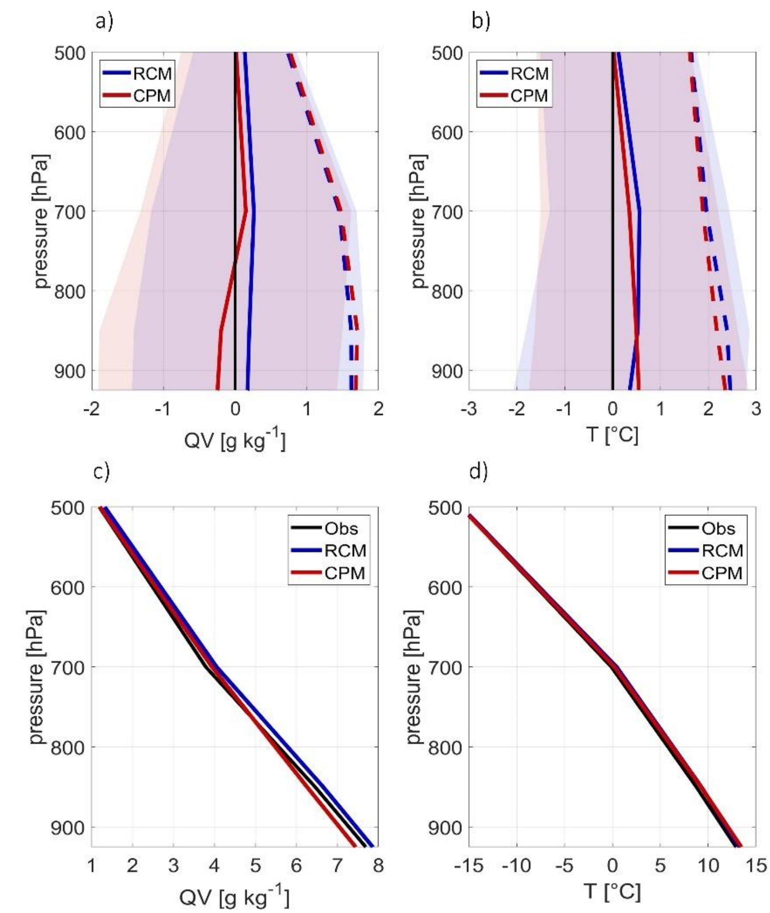

Figure 7. (a, b) Mean bias (solid line), standard deviation of the differences (shaded areas) and RMSE (dashed lines). (c, d) Humidity and temperature profiles of RCM, CPM, and the observations. Radiosondes obtained from the UWYO soundings at Nimes (France); Oppin, Meiningen, Idar-Oberstein, Stuttgart, Kümmersbruck and Munich (Germany); Praha (Czech Republic); Milano, S. Pietro, and Pratica di Mare (Italy). The model information is interpolated to the station location.

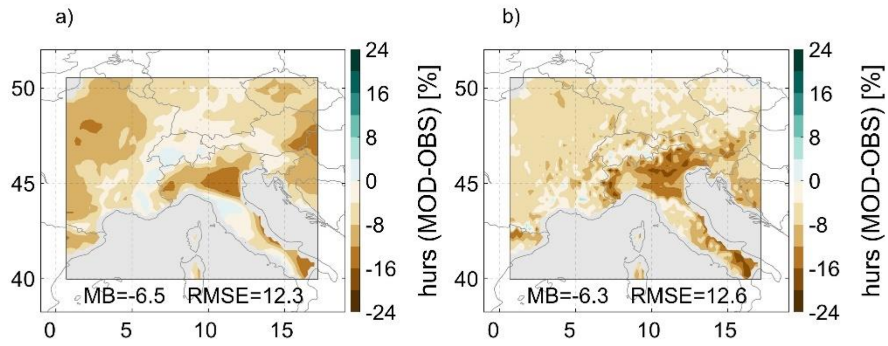

Figure 8. Spatial distributions of the surface specific humidity Mean Bias (MB), obtained as differences between (a) RCM and EOBS-25km and (b) between CPM and EOBS-25km. All datasets have been coarse-grained to a 25 km resolution common grid. The spatially averaged MB and Root Mean Squared Error (RMSE) is shown in text.

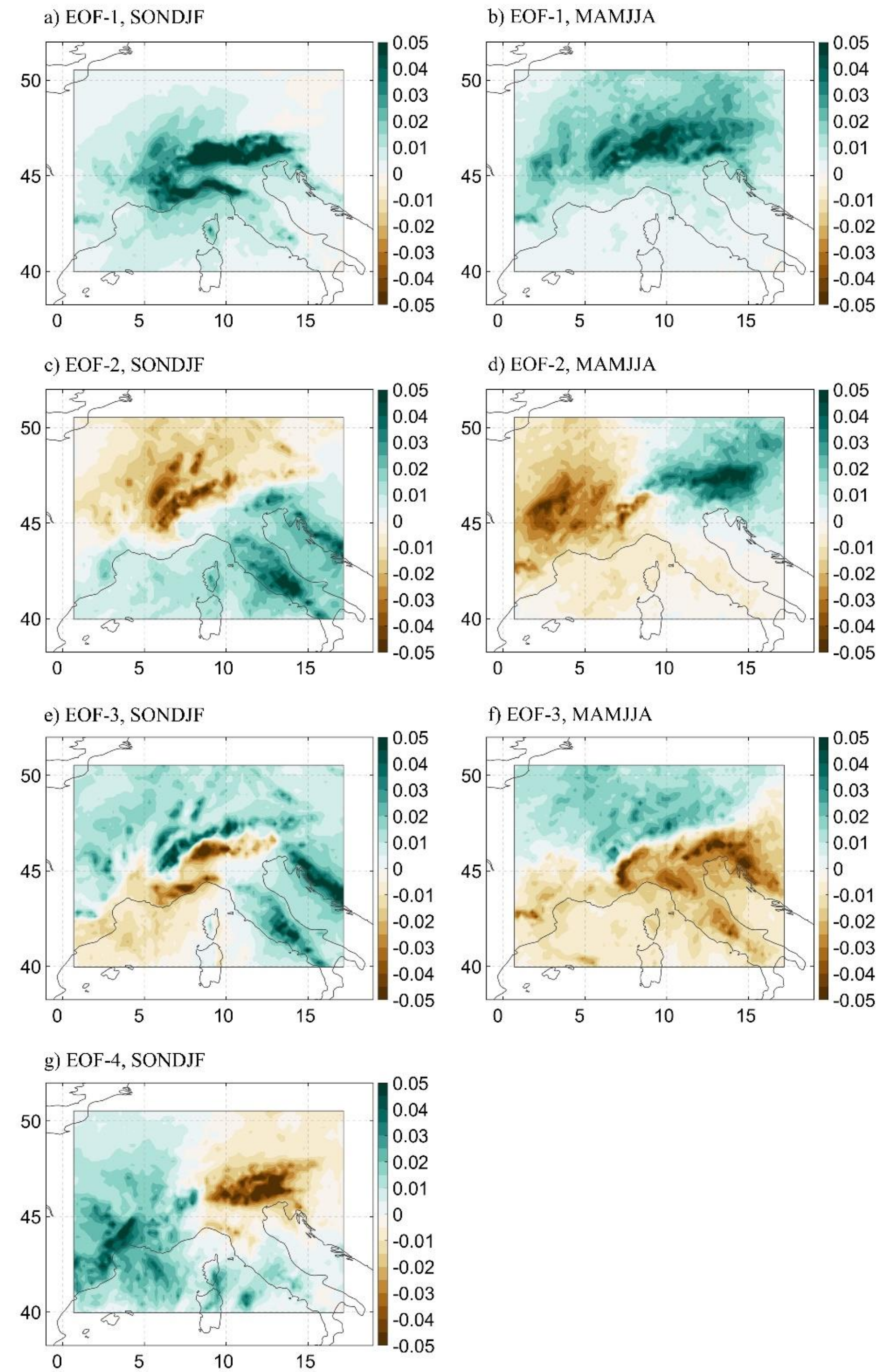

Figure 9. Empirical Orthogonal Functions of precipitation for SONDJF (a, c, e, g) and MAMJJA (b, d, f) events in CPM. The EOFs are obtained using the 290 most severe heavy precipitation events in each season (90-percentile).

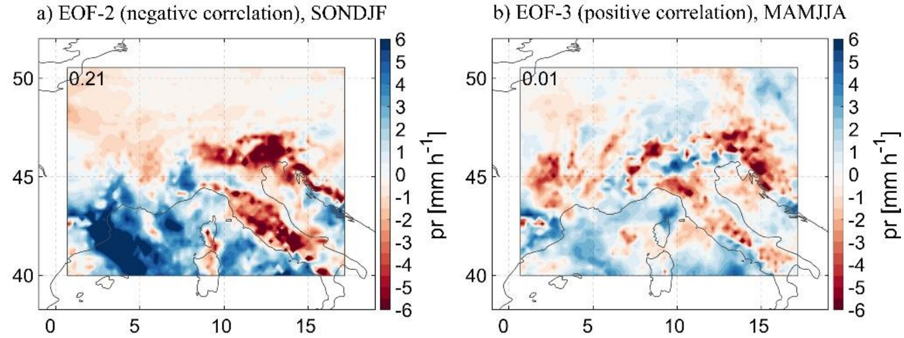

Figure 10. Composite precipitation differences between RCM (blue, positive) and CPM (red, negative). a) composites derived using the heavy precipitation days with the largest negative correlation with winter (SONDJF) EOF-2 (Fig. 9c). b) composites derived using the heavy precipitation days with the largest negative correlation with summer (MAMJJA) EOF-3 (Fig. 9f)

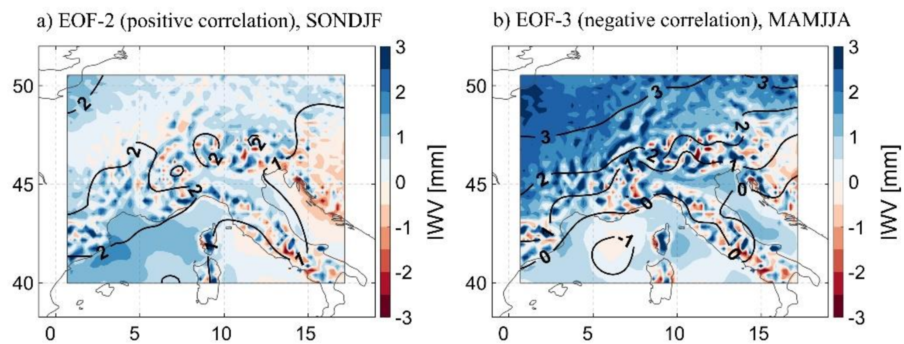

Figure 11. As Fig. 10 but for composite Integrated Water Vapour (IWV) and θ_e^{850} differences between RCM (blue, positive) and CPM (red, negative). The IWV differences are shown in a colour shading and the θ_e^{850} differences as contours. a) extended winter (SONDJF), negative correlation of EOF-2 (Fig. 9c), b) extended summer (MAMJJA), positive correlation of EOF-3 (Fig. 9f).

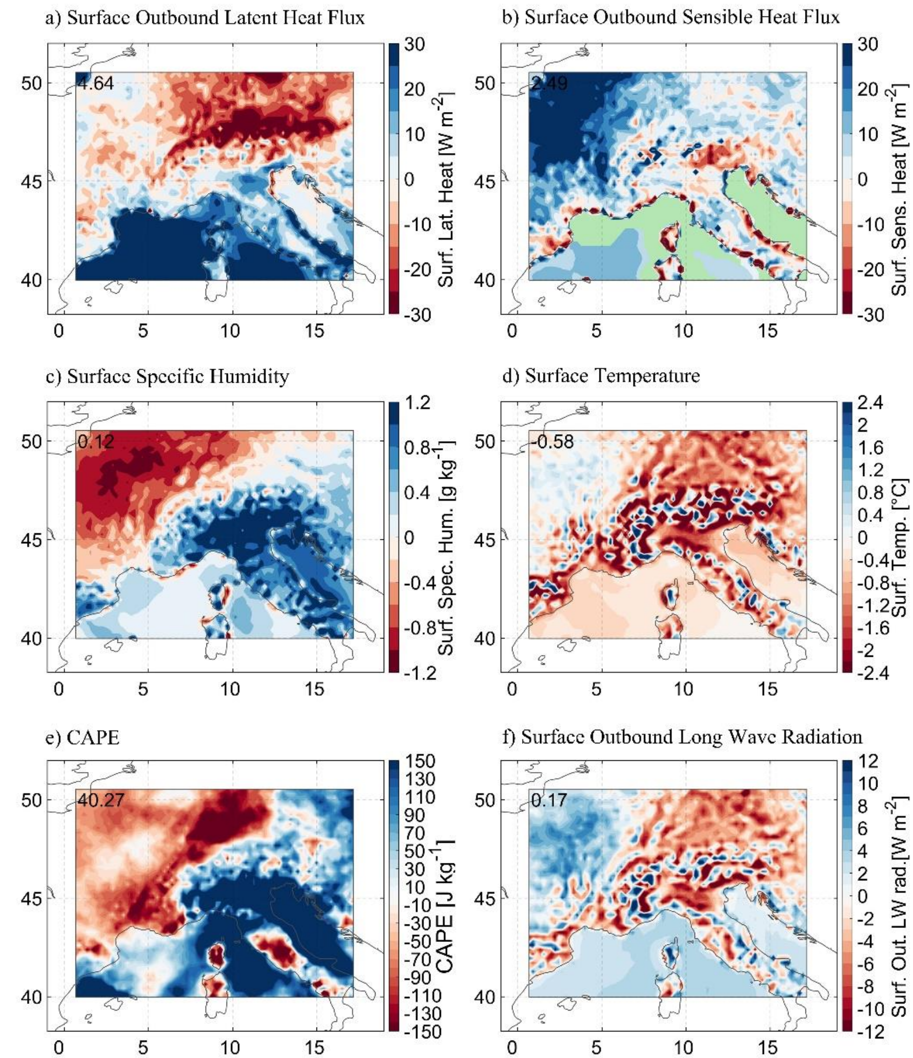

Figure 12. Composite precipitation differences between RCM (blue, positive) and CPM (red, negative). All composites correspond to the positive principal components of EOF-2 in summer (MAMJJA) events. (a) Surface outbound latent heat flux, (b) Surface outbound sensible heat flux, (c) Surface specific humidity, (d) Surface Temperature, (e) CAPE, (f) Surface outbound long wave radiation. Green colours in Latent and Sensible heat fluxes denote inbound directed fluxes and are thus not shown.

Table 1. Description of observational data sets used for validation. The observational data types used to create the products are Radar (R), Gauges (G), Satellites (S), and Reanalysis (R).

Name	Vers.	Res.	Per.	Observations	Provider	Reference	Cover.
EOBS-25km	v20.0e	25 km, daily	1950-2020	Rain Gauges (G), surf. rel. humidity	ECAD	Cornes et al., (2018)	Europe
HYRAS-5km	v2	5 km, daily	1951-2015	Rain Gauges (G)	DWD & BfG	Rauthe et al., (2013), Razafimaharo et al. (2020)	Germany
MSWEP-11km	v2.2.0	11 km, 3-hly	1979-2020	CPC (G), GPCC (G), CMORPH (S), TMPA-3B42RT (S), GSMaP (S), ERA-Interim (R), JRA-55 (R)	GloH2O	Beck et al., (2017)	Global
UWYO	-	Stat., 12 hly	2000-2015	Radiosondes	Wyoming Univers.	http://weather.uwyo.edu/upperair/sounding.html	Global

Table 2. Reanalysis-driven COSMO-CLM decadal simulations.

Name	Res.	Param. Schemes	Lev.	Forcing	Period	Project
RCM[(1)]	25 km, 3-hly	Version. cosmo5.0_clm9. Shallow and deep convection (Tiedtke, 1989)	40	ERA-40	1961-1979	Miklip-II
				ERA-int	1980-2018	
CPM[(2)]	3 km, 1-hly	Version cosmo5.0_clm14. Shallow convection (Tiedtke, 1989). Lake param. (FLAKE; Mironov et al., 2010).	50	ERA-int	2000-2015	FPS-Convection
KLIWA-2.8km[(3)]	2.8 km, 1-hly	Version cosmo5.0_clm3 Only shallow convection parametrized, no lake	49	ERA-40	1971-1999	KLIWA

[1] Domain covers from the Atlantic the eastern Mediterranean from the Maghreb area to Island and Scandinavia.
[2] Domain covers France, northern Italy, Switzerland, the Czech Republic, southern Germany, and the Mediterranean.
[3] Simulations provided by the KLIWA project (www.kliwa.de: Hundhausen et al., 2022). Domain covers southern Germany, Switzerland, and the eastern Czech Republic.

Table 3. Selected heavy precipitation events by means of the PSI between 2000-2015 including the PSI values, total precipitation, maximum grid point precipitation and coverage (percentage of area affected by precipitation over the 80th percentile) are obtained from HYRAS-5km.

Event	Event days	Total. Precip. [mm]	Max. prec. [mmd^{-1}]	Coverage [%]	PSI	WT
15-Jul-2001	12-16 Jul	81098	141	83	2.22	S2
03-Nov-2002	2-5 Nov	80592	52	96	2.55	W4
13-Jan-2004	11-15 Jan	97706	103	97	3.62	W4
22-Aug-2005	19-23 Aug	106852	177	80	2.31	S4
08-Aug-2007	07-09 Aug	85473	95	89	2.79	S1
31-May-2013	31 May-02 Jun	77958	99	94	3.24	S1
08-Jul-2014	06-13 Jul	155621	83	99	3.21	S1

20-Nov-2015	19-21 Nov	102747	109	82	2.83	W1

665 **Table 4. Relative differences of spatially and temporally aggregated precipitation ($RR_{rel.diff.}$) between the model and observations for the duration of each event (see Tab. 3), calculated as $(RR_{mod} - RR_{obs})/RR_{obs}$. The negative signs imply an underestimation of precipitation in the model. FSS is the Fractions Skill Score between the model and the observations (Sect. 2.3.3). MSWEP-11km is used as reference. The best scores are shown for FSS values closer to 1.**

	$RR_{rel.diff.}$ [%]		FSS	
Event	RCM	CPM	RCM	CPM
15-Jul-2001	-40	-34	0.63	0.78
03-Nov-2002	-16	-11	0.81	0.82
13-Jan-2004	-7	-1	0.97	0.97
22-Aug-2005	-28	-26	0.88	0.83
08-Aug-2007	-52	-66	0.63	0.33
31-May-2013	-44	-5	0.26	0.87
08-Jul-2014	-6	-21	0.96	0.9
20-Nov-2015	-18	-17	0.92	0.93

10 Code availability

The COSMO-CLM is available for member of the CLM community and the documentation is accessible at, http://www.cosmo-model.org/content/model/documentation/core/default.htm (last accessed, 11-Aug-2021).

11 Data availability

The EOBS-25km dataset is accessible after registration at https://www.ecad.eu/download/ensembles/download.php#version (last accessed, 17-Dec-2021). The HYRAS-5km data set is publicly accessible at the Climate Data Centre (CDC) of the German Weather Service (DWD) at https://opendata.dwd.de/climate_environment/CDC (last accessed, 17-Dec-2021). MSWEP-11km, has been provided by the Climate Prediction Centre, after agreement of use. The soundings from UWYO are publicly accessible at http://weather.uwyo.edu/upperair/sounding.html (last accessed, 17-Dec-2021). Further information about the XCES tool can be found in (https://www.xces.dkrz.de/)

12 Author contribution

ACA, HF, and JGP designed the study. ELE implemented the PSI index in the Mistral at the DKRZ. ACA and HF analysed the data. ACA prepared the figures and wrote the initial draft. All authors contributed with discussions and revisions.

13 Competing interests

The authors declare that they have no conflict of interest.

14 Acknowledgements

The research was accomplished within project A1 "SEVERE - Scale Dependent Process Representation and Sensitivity Analysis for Most Extreme Events" (Grant No. 01 LP 1901 A) and D2 “COSOX – Coordination of Software Management” (Grant No. 01 LP 1904 B) within the German Federal Ministry of Education and Research (BMBF) research initiative ClimXtreme. JGP thanks the AXA research fund for support. We would like to thank Deborah Niermann and Stella Steidl at the (German Weather Service, DWD) for providing the HYRAS data set. We would like to thank Hylke Beck for sharing the MSWEP precipitation data. Moreover, we would like to acknowledge M. Lemus-Canovas for providing the SynoptReg R package used for computing the synoptic weather types (Lemus-Canovas et al., 2019). We acknowledge the contribution of the DKRZ for storing and maintaining the model data and the FUB for the software coordination of XCES.

15 References

Alfieri, L., Feyen, L., Salamon, P., Thielen, J., Bianchi, A., Dottori, F., and Burek, P.: Modelling the socio-economic impact of river floods in Europe, Natural Hazards and Earth System Sciences, 16, 1401–1411, https://doi.org/10.5194/nhess-16-1401-2016, 2016.

Ban, N., Schmidli, J., and Schär, C.: Evaluation of the convection-resolving regional climate modeling approach in decade-long simulations, Journal of Geophysical Research: Atmospheres, 119, 7889–7907, https://doi.org/10.1002/2014jd021478, 2014.

Ban, N., Rajczak, J., Schmidli, J., and Schär, C.: Analysis of Alpine precipitation extremes using generalized extreme value theory in convection-resolving climate simulations, Climate Dynamics, 55, 61–75, https://doi.org/10.1007/s00382-018-4339-4, 2018.

Ban, N., Caillaud, C., Coppola, E., Pichelli, E., Sobolowski, S., Adinolfi, M., Ahrens, B., Alias, A., Anders, I., Bastin, S., Beluši´c, D., Berthou, S., Brisson, E., Cardoso, R. M., Chan, S. C., Christensen, O. B., Fernández, J., Fita, L., Frisius, T., Gašparac, G., Giorgi, F., Goergen, K., Haugen, J. E., Hodnebrog, Ø., Kartsios, S., Katragkou, E., Kendon, E. J., Keuler, K., Lavin-Gullon, A., Lenderink, G., Leutwyler, D., Lorenz, T., Maraun, D., Mercogliano, P., Milovac, J., Panitz, H.-J., Raffa, M., Remedio, A. R., Schär, C., Soares, P. M. M., Srnec, L., Steensen, B. M., Stocchi, P., Tölle, M. H., Truhetz, H., Vergara-Temprado, J., de Vries, H., Warrach-Sagi, K., Wulfmeyer, V., and Zander, M. J.: The first multi-model ensemble of regional climate simulations at kilometer-scale resolution, part I: evaluation of precipitation, Climate Dynamics, 57, 275–302, https://doi.org/10.1007/s00382-021-05708-w, 2021.

Baldauf, M., Seifert, A., Förstner, J., Majewski, D., Raschendorfer, M., and Reinhardt, T.: Operational convective-scale numerical weather prediction with the COSMO model: Description and sensitivities, Mon. Weather Rev., 139, 3887–3905, https://doi.org/10.1175/MWR-D-10-05013.1, 2011 .

Bandhauer, M., Isotta, F., Lakatos, M., Lussana, C., Båserud, L., Izsák, B., Szentes, O., Tveito, O. E., and Frei, C.: Evaluation of daily precipitation analyses in E-OBS (v19.0e) and ERA5 by comparison to regional high-resolution datasets in European regions, International Journal of Climatology, https://doi.org/10.1002/joc.7269, 2021.

Barthlott, C. and Hoose, C.: Spatial and temporal variability of clouds and precipitation over Germany: multiscale simulations across the &quotgray zone&quot, Atmospheric Chemistry and Physics, 15, 12 361–12 384, https://doi.org/10.5194/acp-15-12361-2015, 2015.

Bastin, S., Drobinski, P., Chiriaco, M., Bock, O., Roehrig, R., Gallardo, C., Conte, D., Alonso, M. D., Li, L., Lionello, P., and Parracho, A. C.: Impact of humidity biases on light precipitation occurrence: observations versus simulations, Atmospheric Chemistry and Physics, 19, 1471–1490, https://doi.org/10.5194/acp-19-1471-2019, 2019.

Beck, H. E., van Dijk, A. I. J. M., Levizzani, V., Schellekens, J., Miralles, D. G., Martens, B., and de Roo, A.: MSWEP: 3-hourly 0.25° global gridded precipitation (1979–2015) by merging gauge, satellite, and reanalysis data, Hydrology and Earth System Sciences, 21, 589–615, https://doi.org/10.5194/hess-21-589-2017, 2017.

Beck, H. E., Pan, M., Roy, T., Weedon, G. P., Pappenberger, F., van Dijk, A. I. J. M., Huffman, G. J., Adler, R. F., and Wood, E. F.: Daily evaluation of 26 precipitation datasets using Stage-IV gauge-radar data for the CONUS, Hydrology and Earth System Sciences, 23, 207–224, 2019.

Berg, P., Christensen, O. B., Klehmet, K., Lenderink, G., Olsson, J., Teichmann, C., and Yang, W.: Summertime precipitation extremes in a EURO-CORDEX 0.11° ensemble at an hourly resolution, Natural Hazards and Earth System Sciences, 19, 957–971, https://doi.org/10.5194/nhess-19-957-2019, 2019.

Berthou, S., Kendon, E. J., Chan, S. C., Ban, N., Leutwyler, D., Schär, C., and Fosser, G.: Pan-European climate at convection-permitting scale: a model intercomparison study, Climate Dynamics, 55, 35–59, https://doi.org/10.1007/s00382-018-4114-6, 2018.

Berthou, S., Rowell, D. P., Kendon, E. J., Roberts, M. J., Stratton, R. A., Crook, J. A., and Wilcox, C.: Improved climatological precipitation characteristics over West Africa at convection-permitting scales, Climate Dynamics, 53, 1991–2011, https://doi.org/10.1007/s00382-019-04759-4, 2019.

Bui, H. X., Yu, J.-Y., and Chou, C.: Impacts of model spatial resolution on the vertical structure of convection in the tropics, Climate Dynamics, 52, 15–27, https://doi.org/10.1007/s00382-018-4125-3, 2018.

Caldas-Alvarez, A. and Khodayar, S.: Assessing atmospheric moisture effects on heavy precipitation during HyMeX IOP16 using GPS nudging and dynamical downscaling, Natural Hazards and Earth System Sciences, 20, 2753–2776, https://doi.org/10.5194/nhess-202753-2020, 2020.

Caldas-Alvarez, A., Khodayar, S., and Knippertz, P.: The impact of GPS and high-resolution radiosonde nudging on the simulation of heavy precipitation during HyMeX IOP6, Weather and Climate Dynamics, 2, 561–580, https://doi.org/10.5194/wcd-2-561-2021, 2021.

Chan, S. C., Kendon, E. J., Fowler, H. J., Blenkinsop, S., Ferro, C. A. T., and Stephenson, D. B.: Does increasing the spatial resolution of a regional climate model improve the simulated daily precipitation?, Climate Dynamics, 41, 1475–1495, https://doi.org/10.1007/s00382-012-1568-9, 2012.

Ciesielski, P. E., Yu, H., Johnson, R. H., Yoneyama, K., Katsumata, M., Long, C. N., Wang, J., Loehrer, S. M., Young, K., Williams, S. F., Brown, W., Braun, J., and Hove, T. V.: Quality-Controlled Upper-Air Sounding Dataset for DYNAMO/CINDY/AMIE: Development and Corrections, Journal of Atmospheric and Oceanic Technology, 31, 741–764, https://doi.org/10.1175/jtech-d-13-00165.1, 2014.

Coppola, E., Sobolowski, S., Pichelli, E., Raffaele, F., Ahrens, B., Anders, I., Ban, N., Bastin, S., Belda, M., Belusic, D., Caldas-Alvarez, A., Cardoso, R. M., Davolio, S., Dobler, A., Fernandez, J., Fita, L., Fumiere, Q., Giorgi, F., Goergen, K., Güttler, I., Halenka, T., Heinzeller, D., Hodnebrog, Ø., Jacob, D., Kartsios, S., Katragkou, E., Kendon, E., Khodayar, S., Kunstmann, H., Knist, S., Lavín-Gullón, A., Lind, P., Lorenz, T., Maraun, D., Marelle, L., van Meijgaard, E., Milovac, J., Myhre, G., Panitz, H.-J., Piazza, M., Raffa, M., Raub, T., Rockel, B., Schär, C., Sieck, K., Soares, P. M. M., Somot, S., Srnec, L., Stocchi, P., Tölle, M. H., Truhetz, H., Vautard, R., de Vries, H., and Warrach-Sagi, K.: A first-of-its-kind multi-model convection permitting ensemble for investigating convective phenomena over Europe and the Mediterranean, Climate Dynamics, 55, 3–34, https://doi.org/10.1007/s00382-018-4521-8, 2018.

Cornes, R. C., van der Schrier, G., van den Besselaar, E. J. M., and Jones, P. D.: An Ensemble Version of the E-OBS Temperature and Precipitation Data Sets, Journal of Geophysical Research: Atmospheres, 123, 9391–9409, https://doi.org/10.1029/2017jd028200, 2018.

Doswell, C. A., Brooks, H. E., and Maddox, R. A.: Flash Flood Forecasting: An Ingredients-Based Methodology, Weather and Forecasting, 11, 560–581, https://doi.org/10.1175/1520-0434(1996)011<0560:fffaib>2.0.co;2, 1996.

Du, Y., Wang, D., Zhu, J., Lin, Z., and Zhong, Y.: Intercomparison of multiple high-resolution precipitation products over China: Climatology and extremes, Atmospheric Research, 278, 106342, 2022.

Emanuel, K. A.: Atmospheric Convection, OXFORD UNIV PR, https://www.ebook.de/de/product/3606238/kerry_a_emanuel_atmospheric convection.html, 1994.

Feldmann, H., g. Pinto, J., Laube, N., Uhlig, M., Moemken, J., Pasternack, A., Früh, B., Pohlmann, H., and Kottmeier, C.: Skill and added value of the MiKlip regional decadal prediction system for temperature over Europe, Tellus A: Dynamic Meteorology and Oceanography, 71, 1618 678, https://doi.org/10.1080/16000870.2019.1618678, 2019.

Fosser, G., Khodayar, S., and Berg, P.: Benefit of convection permitting climate model simulations in the representation of convective precipitation, Climate Dynamics, 44, 45–60, https://doi.org/10.1007/s00382-014-2242-1, 2014.

Fuchs, T., Rapp, J., and Rudolf, B.: Starkniederschläge im Oktober 1998 in Mittel- undWesteuropa, Special report, German Weather Service (DWD), 1998.

Golubev, V., 1986: On the problem of standard condition for precipitation gauge installation. Proceedings of the International Workshop on the Correction of Precipitation Measurements, B. Sevruk, Ed., ETH Zurich, Zürcher Geographische Schriften, Vol. 23, 61–64.

Goodison, B., Louie P. , and Yang D. , 1997: The WMO Solid Precipitation Measurement Intercomparison. IOM Rep. 67, WMO/TD 872, WMO, 211 pp. [Available online at https://www.wmo.int/pages/prog/www/IMOP/publications/IOM-67-solid-precip/WMOtd872.pdf.]

Groisman, P. Y., and Legates D. R. , 1994: The accuracy of United States precipitation data. Bull. Amer. Meteor. Soc., 75, 215–227, doi:10.1175/1520-0477(1994)075<0215:TAOUSP>2.0.CO;2.

Hackenbruch, J., Schädler, G., and Schipper, J. W.: Added value of high-resolution regional climate simulations for regional impact studies, Meteorologische Zeitschrift, 25, 291–304, https://doi.org/10.1127/metz/2016/0701, 2016.

Heim, C.: The Influence of the Resolution of Topography and Surface Fields on the Simulation of Orographic Moist Convection, https://doi.org/10.3929/ETHZ-B-000288269, 2018.

Heim, C., Panosetti, D., Schlemmer, L., Leuenberger, D., and Schär, C.: The Influence of the Resolution of Orography on the Simulation of Orographic Moist Convection, Monthly Weather Review, 148, 2391–2410, https://doi.org/10.1175/mwr-d-19-0247.1, 2020.

Hohenegger, C., Brockhaus, P., Bretherton, C. S., and Schär, C.: The Soil Moisture–Precipitation Feedback in Simulations with Explicit and Parameterized Convection, Journal of Climate, 22, 5003–5020, https://doi.org/10.1175/2009jcli2604.1, 2009.

Holton, J.: An introduction to dynamic meteorology, Academic Press, Amsterdam Boston, 2013.

Hu, G. and Franzke, C. L. E.: Evaluation of Daily Precipitation Extremes in Reanalysis and Gridded Observation-Based Data Sets Over Germany, Geophysical Research Letters, 47, https://doi.org/10.1029/2020gl089624, 2020.

Hundhausen, M., Feldmann, H., Laube, N., and Pinto, J. G.: Future heat extremes and impacts in a convection permitting climate ensemble over Germany, Nat. Hazards Earth Syst. Sci. Discuss. [preprint], https://doi.org/10.5194/nhess-2022-283, in review, 2022.

Jacob, D., Petersen, J., Eggert, B., Alias, A., Christensen, O. B., Bouwer, L. M., Braun, A., Colette, A., Déqué, M., Georgievski, G., Georgopoulou, E., Gobiet, A., Menut, L., Nikulin, G., Haensler, A., Hempelmann, N., Jones, C., Keuler, K., Kovats, S., Kröner, N., Kotlarski, S., Kriegsmann, A., Martin, E., van Meijgaard, E., Moseley, C., Pfeifer, S., Preuschmann, S., Radermacher, C., Radtke, K., Rechid, D., Rounsevell, M., Samuelsson, P., Somot, S., Soussana, J.-F., Teichmann, C., Valentini, R., Vautard, R., Weber, B., and Yiou, P.: EURO-CORDEX: new high-resolution climate change projections for European impact research, Regional Environmental Change, 14, 563–578, https://doi.org/10.1007/s10113-013-0499-2, 2013.

Jolliffe, I. T.: Principal Component Analysis, Springer-Verlag GmbH, New York, https://www.ebook.de/de/product/2047838/i_t_jolliffe_principal_component_analysis.html, 2002.

Kautz, L.-A., Martius, O., Pfahl, S., Pinto, J. G., Ramos, A. M., Sousa, P. M., and Woollings, T.: Atmospheric Blocking and Weather Extremes over the Euro-Atlantic Sector – A Review, Weather Clim. Dynam. Discuss. [preprint], https://doi.org/10.5194/wcd-2021-56, in review, 2021.

Keil, C., Chabert, L., Nuissier, O., and Raynaud, L.: Dependence of predictability of precipitation in the northwestern Mediterranean coastal region on the strength of synoptic control, Atmospheric Chemistry and Physics, 20, 15 851–15 865, https://doi.org/10.5194/acp-20-15851- 2020, 2020.

Kelemen, F. D., Ludwig, P., Reyers, M., Ulbrich, S., and Pinto, J. G.: Evaluation of moisture sources for the Central European summer flood of May/June 2013 based on regional climate model simulations, Tellus A: Dynamic Meteorology and Oceanography, 68, 29 288, https://doi.org/10.3402/tellusa.v68.29288, 2016.

Kendon, E. J., Roberts, N. M., Senior, C. A., and Roberts, M. J.: Realism of Rainfall in a Very High-Resolution Regional Climate Model, Journal of Climate, 25, 5791–5806, https://doi.org/10.1175/jcli-d-11-00562.1, 2012.

Khodayar, S., Davolio, S., Girolamo, P. D., Brossier, C. L., Flaounas, E., Fourrie, N., Lee, K.-O., Ricard, D., Vie, B., Bouttier, F., Caldas-Alvarez, A., and Ducrocq, V.: Overview towards improved understanding of the mechanisms leading to heavy precipitation in the western Mediterranean: lessons learned from HyMeX, Atmospheric Chemistry and Physics, 21, 17 051–17 078, https://doi.org/10.5194/acp-21-17051-2021, 2021.

Knippertz, P., Christoph, M. & Speth, P. Long-term precipitation variability in Morocco and the link to the large-scale circulation in recent and future climates. Meteorol Atmos Phys 83, 67–88 (2003). https://doi.org/10.1007/s00703-002-0561-y

Langhans, W., Schmidli, J., and Schär, C.: Mesoscale Impacts of Explicit Numerical Diffusion in a Convection-Permitting Model, Monthly Weather Review, 140, 226–244, https://doi.org/10.1175/2011mwr3650.1, 2012.

Leckebusch, G. C., Renggli, D., and Ulbrich, U.: Development and application of an objective storm severity measure for the Northeast Atlantic region, Meteorologische Zeitschrift, 17, 575–587, https://doi.org/10.1127/0941-2948/2008/0323, 2008.

Lemus-Canovas, M., Lopez-Bustins, J. A., Trapero, L., and Martin-Vide, J.: Combining circulation weather types and daily precipitation modelling to derive climatic precipitation regions in the Pyrenees, Atmospheric Research, 220, 181–193, https://doi.org/10.1016/j.atmosres.2019.01.018, 2019.

Leutwyler, D., Imamovic, A. and Schär, C. (2021). The Continental-Scale Soil Moisture– Precipitation Feedback in Europe with Parameterized and Explicit Convection, Journal of Climate, 34(13), 5303-5320.

Li, P., Furtado, K., Zhou, T., Chen, H., and Li, J.: Convection-permitting modelling improves simulated precipitation over the central and eastern Tibetan Plateau, Quarterly Journal of the Royal Meteorological Society, 147, 341–362, https://doi.org/10.1002/qj.3921, 2020.

Lin, C., Chen, D., Yang, K., and Ou, T.: Impact of model resolution on simulating the water vapor transport through the central Himalayas: implication for models' wet bias over the Tibetan Plateau, Climate Dynamics, 51, 3195–3207, https://doi.org/10.1007/s00382-018-4074-x, 2018.

Lucas-Picher, P., Argüeso, D., Brisson, E., Tramblay, Y., Berg, P., Lemonsu, A., Kotlarski, S., and Caillaud, C.: Convection -permitting modeling with regional climate models: Latest developments and next steps, WIREs Climate Change, 12, https://doi.org/10.1002/wcc.731, 2021.

Massacand, A. C., Wernli, H., and Davies, H. C.: Heavy precipitation on the alpine southside: An upper-level precursor, Geophysical Research Letters, 25, 1435–1438, https://doi.org/10.1029/98gl50869, 1998.

Meredith, E. P., Maraun, D., Semenov, V. A., and Park, W.: Evidence for added value of convection-permitting models for studying changes in extreme precipitation, Journal of Geophysical Research: Atmospheres, 120, 12 500–12 513, https://doi.org/10.1002/2015jd024238, 2015a.

Meredith, E. P., Semenov, V. A., Maraun, D., Park, W., and Chernokulsky, A. V.: Crucial role of Black Sea warming in amplifying the 2012 Krymsk precipitation extreme, Nature Geoscience, 8, 615–619, https://doi.org/10.1038/ngeo2483, 2015b

Meredith, E. P., Ulbrich, U., and Rust, H. W.: Subhourly rainfall in a convection-permitting model, Environmental Research Letters, 15, 034 031, https://doi.org/10.1088/1748-9326/ab6787, 2020.

Mironov, D., E. Heise, E. Kourzeneva, B. Ritter, N. Schneider, and A. Terzhevik, 2010: Implementation of the lake parameterisation scheme FLake into the numerical weather prediction model COSMO. Boreal Env. Res., 15, 218–230, http://www.borenv.net/BER/archive/pdfs/ber15/ber15-218.pdf

North, G. R., Moeng, F. J., Bell, T. L., and Cahalan, R. F.: The Latitude Dependence of the Variance of Zonally Averaged Quantities, Monthly Weather Review, 110, 319–326, https://doi.org/10.1175/1520-0493(1982)110<0319:tldotv>2.0.co;2, 1982.

Panosetti, D., Schlemmer, L., and Schär, C.: Convergence behavior of idealized convection-resolving simulations of summertime deep moist convection over land, Climate Dynamics, 55, 215–234, https://doi.org/10.1007/s00382-018-4229-9, 2018.

Peña-Guerrero, M. D., Umirbekov, A., Tarasova, L., and Müller, D.: Comparing the performance of high-resolution global precipitation products across topographic and climatic gradients of Central Asia, International Journal of Climatology, 42, 5554–5569, 2022.Peres-Neto, P. R., Jackson, D. A., and Somers, K. M.: How many principal components? stopping rules for determining the number of non-trivial axes revisited, Computational Statistics & Data Analysis, 49, 974–997, https://doi.org/10.1016/j.csda.2004.06.015, 2005.

Pichelli, E., Coppola, E., Sobolowski, S., Ban, N., Giorgi, F., Stocchi, P., Alias, A., Beluši´c, D., Berthou, S., Caillaud, C., Cardoso, R. M., Chan, S., Christensen, O. B., Dobler, A., de Vries, H., Goergen, K., Kendon, E. J., Keuler, K., Lenderink, G., Lorenz, T., Mishra, A. N., Panitz, H.-J., Schär, C., Soares, P. M. M., Truhetz, H., and Vergara-Temprado, J.: The first multi-model ensemble of regional climate simulations at kilometer-scale resolution part 2: historical and future simulations of precipitation, Climate Dynamics, https://doi.org/10.1007/s00382-021-05657-4, 2021.

Pinto, J., Karremann, M., Born, K., Della-Marta, P., and Klawa, M.: Loss potentials associated with European windstorms under future climate conditions, Climate Research, 54, 1–20, https://doi.org/10.3354/cr01111, 2012.

Piper, D., Kunz, M., Ehmele, F., Mohr, S., Mühr, B., Kron, A., and Daniell, J.: Exceptional sequence of severe thunderstorms and related flash floods in May and June 2016 in Germany – Part 1: Meteorological background, Natural Hazards and Earth System Sciences, 16, 2835–2850, https://doi.org/10.5194/nhess-16-2835-2016, 2016.

Prein, A. F., Langhans, W., Fosser, G., Ferrone, A., Ban, N., Goergen, K., Keller, M., Tölle, M., Gutjahr, O., Feser, F., Brisson, E., Kollet, S., Schmidli, J., Lipzig, N. P. M., and Leung, R.: A review on regional convection-permitting climate modeling: Demonstrations, prospects, and challenges, Reviews of Geophysics, 53, 323–361, https://doi.org/10.1002/2014rg000475, 2015.

Prein, A. F., Rasmussen, R., Castro, C. L., Dai, A., and Minder, J.: Special issue: Advances in convection-permitting climate modeling,Climate Dynamics, 55, 1–2, https://doi.org/10.1007/s00382-020-05240-3, 2020.

Preisendorfer, R.: Principal component analysis in meteorology and oceanography, Elsevier Distributors for the U.S. and Canada, Elsevier Science Pub. Co, Amsterdam New York New York, NY, U.S.A, 1988.

Prellberg, D. and Fell, E.: Rheinhochwasser März 1988 Hochwasserablauf und meldedienst, Tech. Rep. 226, Landesamt für Wasserwirtschafft Rheinland Pfalz, 1989.

Purr, C., Brisson, E., and Ahrens, B.: Convective Shower Characteristics Simulated with the Convection-Permitting Climate Model COSMO-CLM, Atmosphere, 10, 810, https://doi.org/10.3390/atmos10120810, 2019.

Rajczak, J., Pall, P., and Schär, C.: Projections of extreme precipitation events in regional climate simulations for Europe and the Alpine Region, Journal of Geophysical Research: Atmospheres, 118, 3610–3626, https://doi.org/10.1002/jgrd.50297, 2013.

Ranasinghe, R., Ruane, A., Vautard, R., Arnell, N., Coppola, E., Cruz, F., Dessai, S., Islam, A., Rahimi, M., RuizCarrascal, D., Sillmann, J., Sylla, M., Tebaldi, C., Wang, W., and Zaaboul, R.: Climate Change Information for Regional Impact and for Risk Assessment. In Climate Change 2021: The Physical Science Basis. Contribution ofWorking Group I to the Sixth Assessment Report of the Intergovernmental Panel on Climate Change [MassonDelmotte, V., P. Zhai, A. Pirani, S.L. Connors, C. Péan, S. Berger, N. Caud, Y. Chen, L. Goldfarb, M.I. Gomis, M.Huang, K. Leitzell, E. Lonnoy, J.B.R. Matthews, T.K. Maycock, T. Waterfield, O. Yelekçi, R. Yu, and B. Zhou (eds.)], Tech. rep., Cambridge University Press, 2021.

Rauthe, M., Steiner, H., Riediger, U., Mazurkiewicz, A., and Gratzki, A.: A Central European precipitation climatology Part I: Generation and validation of a high-resolution gridded daily data set (HYRAS), Meteorologische Zeitschrift, 22, 235–256, https://doi.org/10.1127/0941-2948/2013/0436, 2013.

Razafimaharo, C., Krähenmann, S., Höpp, S., Rauthe, M., and Deutschländer, T.: New high-resolution gridded dataset of daily mean, minimum, and maximum temperature and relative humidity for Central Europe (HYRAS), Theoretical and Applied Climatology, 142, 1531–1553, https://doi.org/10.1007/s00704-020-03388-w, 2020.

Risanto, C. B., Castro, C. L., Moker, J. M., Arellano, A. F., Adams, D. K., Fierro, L. M., and Sosa, C. M. M.: Evaluating Forecast Skills of Moisture from Convective-Permitting WRF-ARW Model during 2017 North American Monsoon Season, Atmosphere, 10, 694, https://doi.org/10.3390/atmos10110694, 2019.

Roberts, N. M. and Lean, H. W.: Scale-Selective Verification of Rainfall Accumulations from High-Resolution Forecasts of Convective Events, Monthly Weather Review, 136, 78–97, https://doi.org/10.1175/2007mwr2123.1, 2008.

Rockel, B., Will, A., and Hense, A.: The regional climate model COSMO-CLM (CCLM), Meteorol. Z., 17, 347–348, https://doi.org/10.1127/0941-2948/2008/0309, 2008. a, b, c

Sangelantoni, L., Sobolowski, S., Lorenz, T. et al. Investigating the representation of heatwaves from an ensemble of km-scale regional climate simulations within CORDEX-FPS convection. Clim Dyn (2023). https://doi.org/10.1007/s00382-023-06769-9, 2022

Schacher, F. and Gerstgrasser, D.: Aussergewöhnliche Gewitterlage im Juni 2007, Technical report, MeteoSchweiz, 2007.

Schäfer, A., Mühr, B., Daniell, J., Ehret, U., Ehmele, F., Küpfer, K., Brand, J., Wisotzky, C., Skapski, J., Rentz, L., Mohr, S., and Kunz, M.: Hochwasser Mitteleuropa, Juli 2021 (Deutschland): 21. Juli 2021 – Bericht Nr. 1 „Nordrhein-Westfalen amp; Rheinland-Pfalz", Tech.rep., https://doi.org/10.5445/IR/1000135730, 2021.

Schättler, U., Doms, G., and Schraff, C.: A Description of the Nonhydrostatic Regional COSMO-Model Part VII: User's Guicd, Tech. rep.,DeutscherWetterdienst, P.O. Box 100465, 63004 Offenbach, Germany, 2016.

Skok, G. and Roberts, N.: Analysis of Fractions Skill Score properties for random precipitation fields and ECMWF forecasts, Quarterly Journal of the Royal Meteorological Society, 142, 2599–2610, https://doi.org/10.1002/qj.2849, 2016.

Sørland, S. L., Brogli, R., Pothapakula, P. K., Russo, E., Van de Walle, J., Ahrens, B., Anders, I., Bucchignani, E., Davin, E. L., Demory, M.-E., Dosio, A., Feldmann, H., Früh, B., Geyer, B., Keuler, K., Lee, D., Li, D., van Lipzig, N. P. M., Min, S.-K., Panitz, H.-J., Rockel, B., Schär, C., Steger, C., and Thiery, W.: COSMO-CLM regional climate simulations in the Coordinated Regional Climate Downscaling Experiment (CORDEX) framework: a review, Geosci. Model Dev., 14, 5125–5154, https://doi.org/10.5194/gmd-14-5125-2021, 2021.

Stucki, P., Rickli, R., Brönnimann, S., Martius, O., Wanner, H., Grebner, D., and Luterbacher, J.: Weather patterns and hydro-climatological precursors of extreme floods in Switzerland since 1868, Meteorologische Zeitschrift, 21, 531–550, https://doi.org/10.1127/0941-2948/2012/368, 2012.

Taylor, C. M., R. A. M. de Jeu, F. Guichard, P. P. Harris, and W. A. Dorigo, 2012: Afternoon rain more likely over drier soils. Nature, 489, 423–426.

Tiedtke, M.: A comprehensive mass flux scheme for cumulus parameterization in large-scale models, Mon. Weather Rev., 117, 1779–1800, https://doi.org/10.1175/1520-0493(1989)117<1779:ACMFSF>2.0.CO;2, 1989.

Toreti, A., Xoplaki, E., Maraun, D., Kuglitsch, F. G., Wanner, H., and Luterbacher, J.: Characterisation of extreme winter precipitation in Mediterranean coastal sites and associated anomalous atmospheric circulation patterns, Natural Hazards and Earth System Sciences, 10, 1037–1050, https://doi.org/10.5194/nhess-10-1037-2010, 2010.

Tramblay, Y., Feki, H., Quintana-Seguí, P., and Guijarro, J. A.: The SAFRAN daily gridded precipitation product in Tunisia (1979–2015), International Journal of Climatology, 39, 5830–5838, https://doi.org/10.1002/joc.6181, 2019.

Ulbrich, U., Christoph, M., Pinto, J. G., and Corte-Real, J.: Dependence of Winter Precipitation Over Portugal on NAO and Baroclinic Wave Activity, International Journal of Climatology, 19, 379–290, 1999.

Uppala, S. M., KÅllberg, P. W., Simmons, A. J., Andrae, U., Bechtold, V. D. C., Fiorino, M., Gibson, J. K., Haseler, J., Hernandez, A., Kelly, G. A., Li, X., Onogi, K., Saarinen, S., Sokka, N., Allan, R. P., Andersson, E., Arpe, K., Balmaseda, M. A., Beljaars, A. C. M., Berg, L. V. D., Bidlot, J., Bormann, N., Caires, S., Chevallier, F., Dethof, A., Dragosavac, M., Fisher, M., Fuentes, M., Hagemann, S., Hólm, E., Hoskins, B. J., Isaksen, L., Janssen, P. A. E. M., Jenne, R., Mcnally, A. P., Mahfouf, J.-F., Morcrette, J.-J., Rayner, N. A., Saunders, R. W., Simon, P., Sterl, A., Trenberth, K. E., Untch, A., Vasiljevic, D., Viterbo, P., and Woollen, J.: The ERA-40 re-analysis, Quarterly Journal of the Royal Meteorological Society, 131, 2961–3012, https://doi.org/10.1256/qj.04.176, 2005.

Vanden-Broucke, S., Wouters, H., Demuzere, M., and van Lipzig, N. P. M.: The influence of convection-permitting regional climate modeling on future projections of extreme precipitation: dependency on topography and timescale, Climate Dynamics, 52, 5303–5324, https://doi.org/10.1007/s00382-018-4454-2, 2018.

Werner, P. and Gerstengarbe, F.-W.: Catalog of the general weather situations of Europe, Potsdam Institute for Climate Impact Research (PIK) , https://www.pik-potsdam.de/en/output/publications/pikreports/.files/pr119.pdf, [online; accessed 10 Nov 2022], 2010.

Xiang, Y., Chen, J., Li, L., Peng, T., and Yin, Z.: Evaluation of Eight Global Precipitation Datasets in Hydrological Modeling, Remote Sensing, 13, 2831, 2021.

Yang, J., Duan, S.-B., Zhang, X., Wu, P., Huang, C., Leng, P., and Gao, M.: Evaluation of Seven Atmospheric Profiles from Reanalysis and Satellite-Derived Products: Implication for Single-Channel Land Surface Temperature Retrieval, Remote Sensing, 12, 791, https://doi.org/10.3390/rs12050791, 2020.